Differential Impact of Multiple Sensory Deprivation on Spatial-coding Cells in Medial Entorhinal Cortex

Jiayi Tian[1, 2], Shidan Wen[1, 2], Yuqian Zhou[1, 2], Shuyang Yao[1, 2], Xuan Zhang[1, 2, 3], Chenglin Miao[1,2,3,4]*

1. State key laboratory of Membrane biology, School of Life Science, Peking university, Beijing, 100871, China
2. PKU-IDG/McGovern Institute for Brain Research, Peking university, Beijing, 100871, China
3. Peking-Tsinghua Center for Life Sciences, Beijing, China
4. Chinese Institute for Brain Research, Beijing (CIBR), China

Chenglin Miao, chenglin.miao@pku.edu.cn

Summary

Spatial navigation depends on anchoring internal spatial maps to external environments, guided by sensory cues such as visual and tactile stimuli. The Medial Entorhinal Cortex (MEC) is crucial for integrating these sensory inputs during the formation of spatial maps. While the responsiveness of many spatial-coding cells to visual stimuli is well-established, the role of tactile sensation in spatial representation is less understood. Rodents primarily gather tactile information through their whiskers, which provide essential spatial and textural details via whisking movements, potentially vital for constructing accurate spatial map. In our study, we employed advanced miniature two-photon microscopy to monitor neural activity in the MEC of freely moving mice subjected to sensory deprivation. Our findings revealed that head direction cells and border cells exhibited impaired spatial representation after either light deprivation or whisker trimming. In contrast, grid cells and speed cells were less affected by whisker trimming compared to visual deprivation, suggesting a stronger dependence on visual cues for these cell types. Notably, distinct subpopulations within each type of spatial-coding cell exhibited varying sensitivity to sensory deprivation—some neurons significantly changed their spatial-coding patterns, while others remained unaffected. This indicates that cells within the MEC may differ in their spatial-coding based on their sensitivity to external sensory inputs. Additionally, we observed a strong correlation between the activity of certain MEC neurons and whisker movement. Collectively, these findings enhance our understanding of how the MEC processes spatial information, particularly in relation to tactile sensation.

Introduction

Spatial navigation depends on the reliable integration of environmental reference cues from various sensory inputs, including visual[1]、auditory[2,3]、olfactory[4] and tactile stimuli[5], into internal spatial maps. This integration is essential for path integration, a critical component of spatial computation[6-8], wherein sensory inputs —especially distant and nearby visual cues like landmarks[8,9] —play a key role. The MEC is specifically involved in path integration, combining internally generated signals such as self-motion, along with

external inputs related to environmental boundaries and landmarks to aid navigation[10-12]. This coordinated process provides the hippocampus with a framework for spatial orientation.

The grid cell, initially characterized by Hafting et al. in 2005, constitutes the first identified spatial-coding cell type within the MEC[13], which exhibit action potentials at locations forming a hexagonal grid pattern. Alongside grid cells, the MEC encompasses other functionally distinct cell types, including head direction cells[14], border cells[15,16], and speed cells[17,18]. It is hypothesized that grid cells play a dominant role in path integration, while head direction cells and speed cells contribute to this process by likely providing self-motion-related information, as suggested by the continuous attractor model.[12]. Additionally, border cells may help correct errors accumulated over time and distance in this process[11] . However, compared to grid cells, other spatial-coding cells in MEC sometimes exhibit different responses when environment changes[19,20] , which implies their respective sensitivity to external sensory input.

Although numerous studies have demonstrated how sensory inputs, particularly visual inputs, influence spatial-coding cells in MEC, such as grid cells and speed cells[20,21], the specific role of tactile inputs in constructing a spatial cognitive map remains largely unexplored. Whiskers, also called facial vibrissae, are the primary tactile organs in rodents and their corresponding bilateral "whisking" behavior playing a crucial role in exploring environment[22]. Trimming animals' whiskers results in impaired performance in spatial learning tasks[23]. And it has been discovered that the hippocampal CA2 region responds to whisker stimulation and is likely involved in the process of updating spatial cognitive maps[24]. Furthermore, the establishment of place fields in the hippocampus is modulated by tactile input, with different cells exhibiting varying response intensities[5]. These findings suggest that spatial map can be constructed using tactile information, encompassing behaviorally relevant spatial elements such as object positions[25], specific boundaries[26,27], and environmental surfaces[28,29]. A strong piece of evidence is that tactile information plays a crucial compensatory role in the absence of visual information when rats are required to complete a gap crossing task in a darkness[27]. However, whether and how the different spatial-coding cell types in MEC respond to tactile inputs remain unclear.

In this study, we examined the alterations in spatial representation within the MEC following light deprivation and whisker trimming. Our findings indicate that distinct spatial-coding cell types exhibit differential responses to these two forms of sensory deprivation. Notably, the strong correlation between whisker movement and the activity of specific MEC neurons may account for the observed changes induced by whisker trimming.

Results

Head-direction tuning in MEC is disrupted by darkness and whisker-trimming

To investigate the influence of visual and tactile inputs on spatial-coding cells in the medial entorhinal cortex (MEC), recombinant adeno-associated virus (rAAV) was used to express

the Ca2+ indicators GCaMP6 in the MEC of the animals (Figure S1). We employed a four-session paradigm consisting of Light, Dark, Dark/Whisker-trimmed, Light/Whisker-trimmed (L-D-DW-LW)—using a cohort of 13 male mice (Figures 1A and S2A). Initially, the mice were allowed to freely explore an open field for approximately 30 minutes under illuminated conditions, establishing a baseline (L). To assess the impact of visual deprivation, the lights were turned off and the mice were allowed to explore the same environment in complete darkness (D). Subsequently, the mice underwent whisker trimming and were reintroduced to the environment, now deprived of both visual and tactile inputs (DW). Finally, the light was turned on to reintroduce visual inputs, enabling assessment of potential recovery (LW). A prism was implanted between the cortex and the cerebellum, enabling the acquisition of calcium signals via a miniature two-photon microscope[30] when mice are freely exploring the open-field (Figures 1B and S1A).

First, we investigated the influence of visual and tactile inputs on head-direction (HD) tuning in the MEC. Calcium traces were extracted from 3,758 neurons, of which 406 (10.8%) were identified as head-direction (HD) cells from baseline and used for further analysis. In the baseline light session, the mean vector length (MVL) of these HD cells was 0.52, with their preferred firing directions (PFD) and the mice's head orientations being nearly uniformly distributed between 0 and 360° (Figures S3A-C). To address potential bias arising from the overrepresentation of cells from a single mouse exhibiting atypical behavior, we applied a linear mixed-effects model (LME) for statistical analysis, incorporating random effects at both the cell and animal levels[31]. This rigorous methodology enabled precise evaluation of the impact of sensory deprivation on HD tuning and was similarly employed to assess changes in the primary features of other cell types. We subsequently calculated the tuning curves of selected HD cells for each experimental session and used LME to perform statistical analysis for the main characteristics. Our analysis revealed that both the MVL and head information (Head Info.) of HD cells were significantly reduced in the dark environment compared to the baseline light condition (Figures 1E-G; L/D; two-sided *t*-test, n = 406, MVL: $P = 1.8 \times 10^{-12}$; Head Info.: $P = 2.2 \times 10^{-8}$). Moreover, the subsequent whisker-trimming procedure further disrupted HD tuning in the MEC. (Figures 1H-J; D/DW; MVL: $P = 5.6 \times 10^{-6}$; Head Info.: $P = 9.3 \times 10^{-10}$). Light deprivation and whisker trimming also led to the change of preferred directions, mean firing rate alterations, and variance in HD tuning correlation across session pairs (Figures S3D-F). Importantly, the animals' behavioral performance and the quality of the imaging data were consistent across all sessions, thereby ruling out the possibility that the observed change in firing patterns was due to these factors (Figures S2B-G). Furthermore, we computed the population vector (PV) correlation for all HD cells between each session pair. The results showed that both darkness and whisker-trimming led to destabilization of population-level HD coding compared with its previous state (Figures 1K-L; n = 13, mean ± SEM: L/D: 0.56 ± 0.03; D/DW: 0.49 ± 0.03).

Differential impact of visual and tactile inputs on HD tuning stability

Previous research has demonstrated that disturbance in thalamic HD tuning caused by

darkness can gradually recover to its initial state with increased experience[32]. To investigate whether this phenomenon is also present in our results and to further elucidate the distinct effects of visual and tactile input deprivation, we segmented each session into several intervals and calculated MVL for each 6-minute time bin. This approach enabled us to monitor the progressive changes in MVL throughout the session. By fitting a linear regression to these MVL data points for each HD cell and calculating the slope, we observed a slight recovery in HD tuning over time in the dark environment (Figure 1M). This suggests that the impact of visual input deprivation may be transient for certain cells, with the possibility that the animals could partially mitigate this loss by re-exploring the environment. In contrast, following whisker trimming, MVL exhibited no signs of recovery, indicating a more persistent disruption of HD tuning in the absence of tactile cues (Figures 1M-N; one-sample *t*-test against 0, L: n = 402, P = 0.41; D: n = 399, P = 0.03; DW: n = 402, P = 0.97).

To further validate these findings, we applied Linear Discriminant Analysis (LDA) to perform dimensional reduction based on the neural activity of HD cells. In the light condition, the neural representations of different head directions were well-separated, demonstrating robust HD tuning under normal sensory conditions (Figure 1O). However, in the dark condition, the separation between head directions diminished, indicating a compromised neural representation due to the absence of visual cues. The disruption was even more pronounced following whisker trimming, where the initial encoding of head direction was nearly entirely disrupted, suggesting that tactile cues play a critical role in maintaining HD cell functionality. Quantitative analysis further confirmed these effects, since both the Fisher's discrimination ratio and the separation index exhibit a significant decline from the light condition to the dark and further to the dark with whisker trimming conditions (Figure 3P; paired *t*-test, n = 9, Fisher's discrimination ratio: L/D:P = 2.1×10^{-5}, D/DW:P = 0.0001; separation index: L/D: P = 0.0006, D/DW: P = 4.5×10^{-5}). These metrics corroborate that the original representation of head direction deteriorates progressively, with the most substantial impairment observed when both visual and tactile inputs are removed.

Furthermore, the performance of HD tuning deteriorated in a subsequent session (LW) where the lights were reactivated (Figures S3G-I; DW/LW; two-sided *t*-test, n = 406, MVL: P = 2.3×10^{-5}; Head Info.: P = 5.7×10^{-4}), indicating the reintroduction of visual cues alone was insufficient to restore HD tuning after both sensory modalities had been deprived. Collectively, these findings indicate that HD tuning in the MEC is highly susceptible to the deprivation of both visual and tactile inputs. Moreover, the data suggest that these two sensory modalities contribute differently to spatial navigation. The internal HD representation of the baseline allocentric reference frame is not completely lost after light deprivation, with tactile inputs exerting a more sustained influence on HD tuning.

Distinct HD cell clusters exhibit differential responses to multiple sensory deprivation

While the previous results demonstrated that HD tuning in MEC was disrupted at the

population level following light deprivation or whisker trimming, scatter plots indicated that some cells remained unaffected after sensory deprivation (Figures 1E and 1H). This observation suggests a significant heterogeneity among HD cells, likely arising from variations in the inputs they receive from other brain regions. To further investigate this heterogeneity, we employed a Gaussian Mixture Model (GMM) to perform unsupervised clustering based on changes in mean vector length (ΔMVL) and HD tuning correlation between session pairs (see Methods). The model achieved optimal performance when HD cells were classified into three distinct clusters, which were visualized through the principal component analysis (PCA) in the first two dimensions (Figure 2A and Figure S4A; see Methods).

The GMM identified three distinct categories of HD cells, each exhibiting unique distributions of changes in preferred firing direction (ΔPFD) between session pairs. The first cluster, termed "sensory-resistant HD cells," showed minimal changes in their preferred directions, regardless of whether the light was turned off or the animals' whiskers were trimmed (Figures 2B-D; L/D: mean ΔPFD: 32°; D/DW: mean ΔPFD: 32°; KS-test, n = 313, P = 0.19; Figure S4E; Wilcoxon test, n = 313, P = 0.07). Their tuning curves remained stable across all sessions (Figure 2C). The second cluster, designated as "whisker-sensitive HD cells," exhibited small changes in preferred direction when visual input was deprived, but significant alterations occurred following whisker trimming (Figures 2B-D; L/D: mean ΔPFD: 25°; D/DW: mean ΔPFD: 77°; KS-test, n = 27, P = 7.7×10^{-4}; Figure S4E; Wilcoxon test, n = 27, P = 3.0×10^{-4}). MVL for this cluster decreased markedly, with some cells losing their HD tuning properties entirely after whisker trimming (Figure 2D). This cluster is primarily responsive to tactile inputs, with a reduced sensitivity to visual inputs. The third cluster, referred to as "sensory-sensitive HD cells," displayed substantial changes in preferred direction following the deprivation of either sensory input (Figures 2B-D; L/D: mean ΔPFD: 64°; D/DW: mean ΔPFD: 66°; KS-test, n = 66, P = 0.99; Figure S4E; Wilcoxon test, n = 66, P = 0.92). This suggests that these cells are modulated by both visual and tactile cues, although it is possible that some cells in this cluster are primarily regulated by visual inputs. The significant differences in ΔPFD among the distinct clusters between certain session pairs further validated our clustering results (Figure S4F; Welch's t-test; L/D: P = 0.23 (Cluster 1 vs. Cluster 2), P = 1.0×10^{-6} (Cluster 1 vs. Cluster 3), P = 5.7×10^{-6} (Cluster 2 vs. Cluster3); D/DW: P = 0.0003 (Cluster 1 vs. 2), P = 6.0×10^{-8} (Cluster 1 vas. Cluster 3), P = 0.38 (Cluster 2 vs. Cluster 3)). Within the total population of HD cells, sensory non-sensitive cells constituted the majority (77.1%), followed by sensory-sensitive cells (16.3%) and whisker-sensitive cells (6.6%) (Figure S4B).

Notably, the MVL of sensory-resistant HD cells during the baseline light session (L) was not significantly higher than that of the other two clusters, suggesting that the observed responses to multisensory deprivation in the other two clusters were not attributable to poor baseline HD tuning (mean ± SEM, Cluster 1: 0.52 ± 0.00; Cluster 2: 0.62 ± 0.03; Cluster 3: 0.48 ± 0.02; Welch's *t*-test, P = 0.0006 (Cluster 1 vs. Cluster 2), P = 0.09 (Cluster

1 vs. Cluster 3), P = 0.0008 (Cluster 2 vs. Cluster 3); Figure S4C). These findings indicate the presence of distinct HD cell clusters in MEC that exhibit differential responses to sensory information (Figure S5). Some HD cells exhibit responsiveness to specific sensory inputs, while others are modulated by multiple sensory inputs. In contrast, certain HD cells remain impervious to external sensory alterations. However, no anatomical clustering tendency was observed within these cell clusters (Figure S4D; Wilcoxon test, n = 12, P = 0.47). This rigorous analysis underscores the heterogeneous nature of HD cells in the MEC, highlighting the varied roles that visual and tactile inputs play in spatial navigation.

To further substantiate our findings, we conducted an additional experiment involving four more mice, in which they completed the two session Light-Light, Whisker-trimmed (L-LW) task. In this experiment, animals' whiskers were trimmed immediately after the light baseline session (L) to proceed with the subsequent session (LW). Our results showed that head direction tuning in the MEC was significantly disrupted by whisker trimming even in the light conditions (Figure S3J; Wilcoxon test, n = 153, MVL:P = 3.0×10^{-16}, Head Info.: P = 1.0×10^{-10}), further confirming that the firing patterns of HD cells are strongly modulated by whisker-supported tactile inputs. Moreover, despite significant alterations in the firing patterns of some cells, a subset of cells maintained stable HD tuning (Figure S3J), consistent with the heterogeneity observed in the previous L-D-DW-LW task.

Border cells in MEC are modulated by both visual and tactile inputs

In addition to HD cells, MEC contains various other types of spatial-coding cells, including border cells, grid cells, speed cells, and spatial cells. We next sought to determine whether border cells in MEC are influenced by visual inputs and whisker-supported tactile inputs. A total of 220 neurons (5.9%) were identified as border cells, with an average border score of 0.63 (Figure S6A). Notably, the presence of border cells in our data was confirmed by the formation of new firing fields when a wall was inserted into the environment the day before the formal experiment (Figure S6D).

Our analysis revealed that border cells exhibited a response pattern similar to that of HD cells. Specifically, both border score and spatial information significantly decreased in the dark condition compared to baseline (Figures 3A-C; L/D; two-sided *t*-test, n = 220, Border score: P = 2.8×10^{-25}; Spatial Info.: P = 0.04). Furthermore, whisker trimming in the dark condition led to an additional decrease in both parameters (Figures 3D-F; D/DW; two-sided *t*-test, n = 220, Border score: P = 0.02; Spatial Info.: P = 4.4×10^{-5}). Additionally, changes were observed in the mean firing rate and spatial tuning map of border cells following either light off or whisker trimming (Figures S6B-C). Border score and spatial information did not improve during the final LW session, indicating that the spatial coding of these cells could not be restored to its initial state after visual inputs were reintroduced (Figures S6H-J; DW/LW; two-sided *t*-test, n = 220, Border score: P = 0.48; Spatial Info.: P = 0.18).

Given the observed heterogeneity in border cell performance, we sought to determine whether these cells could also be clustered based on their responses under different experimental conditions. Using an optimal GMM, we identified two distinct types of border

cells based on spatial correlation between session pairs (Figures 3G and S6E). The first cluster, termed "sensory-resistant border cells," exhibited consistently high spatial correlation regardless of changes in experimental conditions. In contrast, the second cluster, referred to as "sensory-sensitive border cells," displayed relatively lower spatial correlation scores following sensory input deprivation. The former cluster represented the majority of border cells (76.8%), while the latter constituted 23.2% (Figure S6G). Notably, "sensory-resistant border cells" had a slightly higher border score during the baseline session (Figure S6F; mean ± SEM, Cluster 1: 0.64 ± 0.01; Cluster 2: 0.60 ± 0.01; KS-test, n = 169 and n = 51, P = 0.005; Welch's t-test, P = 0.006). Moreover, "sensory-sensitive border cells" exhibited significantly higher changes in border score (Δ border score) between session pairs compared to "sensory-resistant border cells" (Figures 3H-I; L/D: KS-test, n = 169 and n = 51, P = 1.7×10^{-7}; Welch's *t*-test, P = 3.9×10^{-6}; D/DW: KS-test, n = 169 and n = 51, P = 0.03; Welch's *t*-test: P = 0.02). Population vector correlation analysis further demonstrated that "sensory-resistant border cells" maintained a more stable spatial-coding profile when sensory inputs were deprived (Figure 3J; paired *t*-test, n = 12, L/D: P = 4.0×10^{-7}; D/DW: P = 2.9×10^{-5}). These findings indicate that border cells in MEC respond differentially to multisensory inputs, with some cells being modulated by both visual and tactile inputs, while others remain unaffected (Figure S7). Unlike HD cells, we were unable to isolate a cell type affected mainly by one specific sensory input, which may be due to the integrated response of most border cells to multisensory inputs or limitations of our clustering methods and data.

The disruption of spatial representation of border cell population was also observed in the L-LW task(Figures S6K; Wilcoxon test, n = 116, MVL:P = 1.1×10^{-9}, Head Info.: p = 3.4×10^{-4}). Similar to HD cells, some border cells responded to whisker trimming, while others remained unaffected (Figure S6K).

Grid cells are mainly modulated by visual inputs rather than tactile inputs

Grid cells are the predominant type of spatial-coding cells in MEC and have long been regarded as implicating in path integration[12,33]. Historically, grid cells were thought to operate independently of external sensory inputs, generating their characteristic hexagonal firing patterns based solely on self-motion information. However, recent studies have challenged this notion, demonstrating that spatial-coding performance of grid cells is modulated by various sensory inputs, especially by visual cues[10,20].

In our study, we identified 261 grid cells (6.9% of all recorded neurons), with an average grid score of 0.54 (Figure S8A). We observed that the hexagonal firing pattern of some grid cells was disrupted, the overall grid score significantly decreased in darkness, consistent with previous findings[20] (Figures 4A-B; L/D; two-sided *t*-test, n = 261, P = 2.8×10^{-32}), and the spatial information exhibited no significant change, with only slight decreases in mean and median values (Figure 4C; mean ± SEM, L: 1.04 ± 0.02; D: 1.03 ± 0.02; two-sided *t*-test, n = 261, P = 0.70). The mean firing rate and spatial coding of the grid cell population were altered following sensory input deprivation (Figures S8B-C). Notably, the firing

patterns of grid cells remained largely unaffected by whisker trimming (Figures 4D-F; two-sided *t*-test, n = 261, Grid score: P = 0.13; Spatial Info.: P = 0.09), suggesting a small influence of whisker-supported tactile inputs on grid cell function. The original grid pattern did not recover when the mice were reintroduced to the light environment with their whiskers trimmed (Figures S8E-G; DW/LW; two-sided *t*-test, n = 261, Grid score: P = 0.32; Spatial Info.: P = 0.50).

To further validate these findings, we conducted a detailed examination of the firing maps of each grid cell (see Methods). The analysis revealed that, although the average grid spacing remained unchanged between session pairs (Figure 4G; L/D, Wilcoxon test, n = 261, P = 0.26; D/DW, P = 0.64), the grid pattern became less regular in darkness, accompanied by an increase in the standard deviation of grid spacing and ellipticity (Figures 4H-I; Grid ellipticity: Wilcoxon test, n = 175, P = 0.002; SD of Grid spacing: Wilcoxon test, n = 261, P = 8.2×10^{-5}). These parameters remained stable following whisker trimming (Figures 4H-I; Grid ellipticity: Wilcoxon test, n = 180, P = 0.13; SD of Grid spacing: Wilcoxon test, n = 261, P = 0.16). This further confirms the stronger impact of visual inputs compared to tactile inputs on grid cells.

Additionally, we decoded the position based on the population activity of four mice that possessed more than 20 grid cells. The decoding performance improved as the number of participating grid cells increased (Figure S8D). To determine whether the spatial coding of grid cells changes following sensory input deprivation, we compared their performance to baseline conditions. Specifically, we split the baseline light session into two halves. The first half served as the training set, while the second half—along with the second halves of other sessions—was used to construct the test set for each experimental condition. The mean absolute error (MAE) of the decoded position relative to the animals' actual position was significantly lower during the baseline light sessions compared to shuffled results (Figures 4J-K; see Methods). In darkness, the MAE increased compared to the light environment but remained unchanged after whisker trimming (Figure 4K; paired *t*-test, n = 4, Shuffle/L: P = 0.005; L/D: P = 0.007; D/DW: P = 0.92). This suggests that the internal spatial-coding pattern of the original grid cell population was disrupted by the deprivation of visual inputs but remains unaffected by the deprivation of tactile inputs. Notably, despite the sensory deprivation, the decoder across all sessions consistently produced a lower MAE than the shuffled results (Figure 4K). This finding suggests that grid cells retain some ability to construct a cognitive map of the environment even in the absence of visual and tactile inputs, potentially through path integration.

GMM identified two distinct clusters of grid cells based on the correlation of spatial-coding maps between session pairs (Figures 4L and S8J-I), which we termed "sensory-resistant grid cells" and "sensory-sensitive grid cells" (Figures 4L and S9). The “sensory-resistant grid cells” maintained a stable spatial-coding pattern even when external sensory inputs were deprived and exhibited relatively higher within-session stability compared to the “sensory-sensitive grid cells” (Figures 4L-N; KS-test, n = 186 and n = 75, L/D: P = 6.3×10^{-5}; D/DW: P = 0.31; Welch’s *t*-test, n = 186 and n = 75, L/D: P = 2.4×10^{-5}; D/DW: P =

0.15). Additionally, the “sensory-resistant grid cells” demonstrated a more stable population coding pattern than the “sensory-sensitive grid cells” (Figure 4O; paired *t*-test, n = 11, L/D: P = 7.2×10^{-6} ; D/DW: P = 5.0×10^{-7}). Importantly, the difference in Δ stability between the two types of grid cells was observed primarily after the deprivation of visual inputs and was minimally affected by the deprivation of tactile inputs (Figures 4M-N).

Furthermore, we identified 20 conjunctive Grid × HD cells (Figure S4G; see Methods), which were exclusively observed in the “sensory-resistant HD cells” and “sensory-sensitive HD cells”—the only two clusters also identified among grid cells (Figure S4H). Notably, these conjunctive cells exhibited behavior more akin to grid cells than to pure HD cells following multisensory deprivation (Figures S4I-J). In conclusion, our results demonstrate that grid cells are predominantly modulated by visual cues rather than tactile inputs, underscoring the importance of visual information in maintaining the spatial-coding capabilities of grid cells in the medial entorhinal cortex.

Speed cells and spatial cells exhibit similar response as grid cells

Next, we investigated how velocity signals in MEC are modulated by visual and tactile inputs. Previous studies have demonstrated that speed tuning in MEC, similar to grid cells, is responsive to visual cues[20,21]. We identified speed cells in the MEC by correlating instantaneous calcium events with running speed (Method 1). The overall speed score significantly decreased in darkness compared to the baseline light session, but did not further decrease following whisker trimming (Figures 5A-B and 5D-E; L/D; two-sided *t*-test, n = 363, Speed score: P = 1.4×10^{-57}; D/DW: P = 0.12), which is consistent with the behavior of grid cells. Additionally, we employed an alternate approach to calculate the speed score based on the calcium data (Method 2; see Methods) to validate the reliability of our results. Method 2 identified a comparable proportion of speed cells and yielded statistical results consistent with those of Method 1 (Figure S10A).

To further validate these findings, we created speed tuning curves for each speed cell by plotting running speed on the x-axis and the corresponding event rate at each speed interval on the y-axis. By performing a linear regression to these curves and calculating their slopes, we observed a decrease in slope during darkness compared to the light session, indicating a diminished speed-tuning capability within the original speed cell population (Figures 5C; two-sided *t*-test, n = 363, P = 2.0×10^{-38}). Additionally, a slight increase in slope was observed following the whisker-trimming session (Figures 5F; two-sided *t*-test, n = 363, P = 0.01), a phenomenon that was also noted when the lights were turned back on to re-introduce visual input (Figures S10B; two-sided *t*-test, n = 363, Speed score: P = 0.01; Slope: P = 0.001). This slight increase in slope is likely attributable to the animals' adaptation to the experimental arena.

GMM also achieved optimal performance when speed cells were divided into two distinct clusters (Figure S10D) based on the correlation of speed tuning across sessions (Figures 5G and S10C). "sensory-sensitive speed cells" exhibited a significantly higher Δ speed score compared to "sensory-resistant speed cells" following the deprivation of external

sensory inputs, with the most pronounced differences observed in darkness compared to the baseline light session (Figures 5H-I; KS-test, n = 316 and n = 47, L/D: P = 2.5 × 10^{-7}; D/DW: P = 0.72; Welch's *t*-test, n = 316 and n = 47, L/D: P = 4.0 × 10^{-8}; D/DW: P = 0.32). In the "sensory-sensitive" cluster, most speed tuning has already been disrupted when the lights were turned off (Figure 5J and S10E). These findings strongly suggest that, similar to grid cells, speed tuning in the MEC is more influenced by visual inputs than by tactile inputs.

Spatial cells demonstrated responses comparable to those of grid and speed cells. While their spatial-coding were disrupted in darkness, they were less affected by whisker trimming (Figures S11A-D; two-sided *t*-test, n = 482, L/D: P = 2.2 × 10^{-22}; D/DW: P = 0.96). The decoding accuracy of spatial cells also decreased in darkness compared to light condition; however, it did not experience further degradation following whisker trimming (Figure S11E; paired *t*-test, n = 8, Shuffle/L: P = 8 × 10^{-4} ; L/D: P = 0.02; D/DW: P = 0.09), similar to the behavior observed in grid cells. Furthermore, these cells were categorized into two distinct types, each exhibiting different responses to sensory deprivation (Figure S11G-K).

Subgroup of cells in MEC are modulated by whisker movement

During free exploration, rodents use their whiskers bilaterally to interact with objects, providing essential tactile inputs. Previous research has shown that the CA1 region of the hippocampus responds to both mechanical and passive whisker stimulation, potentially contributing to the updating of the spatial cognitive map[24]. Furthermore, it has been established that place fields in the hippocampus are modulated by tactile inputs from whiskers, although there is variability among individual cells[5]. Our earlier results indicated that certain spatial-coding cells in MEC alter their coding in response to the deprivation of tactile inputs caused by whisker-trimming. Consequently, we sought to investigate whether MEC contains cells that respond specially to whisker movement.

We conducted whisker-related experiments using seven male mice, four of which also participated in the L-LW experiments. Each mouse underwent three experimental sessions (Figure 6A). In the "spontaneous-whisking" session, mice were head-fixed, and their spontaneous whisker movements, along with corresponding neuronal activity, were recorded using cameras and a miniature two-photon microscope. Due to minimal whisker movement under head-fixed conditions, we performed an additional "stimulated-whisking" session, during which an automated telescopic rod with a sandpaper sheet at its end was used to enhance whisker activity at regular intervals. In the final "free exploration" session, mice were allowed to explore an open field, enabling us to assess the spatial-coding properties of the neurons recorded in the previous sessions. Given that whiskers on the same side exhibit highly similar movement[34] (Figure S12A), we selected the most distinguishable whisker for each animal for further analysis. To minimize false positives resulting from the low whisker movement observed during the "spontaneous-whisking" session, we primarily used data from the "stimulated-whisking" session to identify whisker-

402 responsive neurons, with the "spontaneous-whisking" session serving to validate our
403 findings. We calculated the Pearson correlation coefficient between whisker movement
404 and the calcium traces for each neuron (see Methods). Neurons with a correlation
405 coefficient exceeding the 95th percentile of the shuffled data were classified as “whisker-
406 sensitive” cells. We opted for this correlation-based approach rather than comparing
407 neuronal activity between stimulated and non-stimulated intervals due to the low temporal
408 resolution of two-photon imaging and the potential for time-delayed responses, which could
409 result in a mismatch between the timing of stimulation and neuronal activity.

410 Of the 1,118 recorded neurons from seven mice, 416 (35%) were identified as "whisker-
411 sensitive” cells, characterized by an increased ΔF/F in response to increased whisker
412 movement (Figures 6B and 6D). These cells’ neuron activity exhibited significantly higher
413 correlations with whisker movement compared to "whisker-non-sensitive” cells (Figure 6C;
414 Welch’s *t*-test, n = 416 and n = 772, $P = 1.3 \times 10^{-154}$) and demonstrated similar performance
415 in the "spontaneous-whisking" session (Figures 6C-E, S12B, and S12E). Of the "whisker-
416 sensitive” cells, 416 (18%) showed spatial-coding properties when the mice freely explored
417 the environment, with HD cells representing the largest proportion (9.9%), followed by
418 border cells (5.8%) and grid cells (2.4%) (Figures 6F-G; Chi-Square test, $P = 9.8 \times 10^{-16}$).
419 To investigate whether these “whisker-sensitive” cells exhibit clustered anatomical
420 distribution, we calculated the pairwise distances between all “whisker-sensitive” cells
421 within each FOV. We then generated a shuffled dataset by randomly assigning the
422 “whisker-sensitive” identity to each cell, repeating this process 1,000 times. The true
423 pairwise distances were compared to the distances from the shuffled dataset to assess the
424 significance of the observed clustering. The result showed that "whisker-sensitive” cells did
425 not exhibit anatomical aggregation within our field of view (Figure S12C-D; Wilcoxon test,
426 n = 7, P = 0.58; see Methods).

427 To further validate our results, we calculated the mutual information (MI)[35] between
428 neuronal activity and whisker movement using their joint probability distribution (see
429 Methods). The identified "whisker-sensitive” cells exhibited higher MI values than "whisker-
430 non-sensitive” cells (Figure S12F, Welch’s *t*-test, n = 415 and n = 772, P = 0.04). In addition,
431 we calculated the conditional probability distribution of neuronal activity given whisker
432 movement and performing a linear regression to the resulting heatmap. The slope for
433 "whisker-sensitive” cells was significantly higher, indicating that their event rates were more
434 positively modulated by whisker movement (Figure S12G; Welch’s *t*-test, n = 416 and n =
435 772, P = 0.02). Notably, spatial-coding cells in the MEC did not exhibit a stronger tuning to
436 whisker movement compared to non-spatial-coding cells (Figures S12H). Within the
437 spatial-coding category, neuron activity of HD cells displayed the highest mean correlation
438 with whisker movement, followed by border cells and grid cells, although these differences
439 were not statistically significant (Figure S12I; mean ± SEM, HD: 0.06 ± 0.01, Border: 0.054
440 ± 0.01, Grid: 0.046 ± 0.01). This observation is consistent with previous findings, which
441 indicated that the deprivation of tactile inputs had a more pronounced effect on HD cells
442 and border cells compared to grid cells.

Discussion

Effective spatial navigation is fundamentally dependent on reliable references, which are derived from both internal and external sensory information[36]. Our findings reveal that tuning of HD cells and border cells in the MEC were significantly influenced by both light deprivation and whisker trimming. However, spatial coding of grid cells and speed coding appeared largely affected by visual sensory input rather than whisker-supported tactile input. Further analysis revealed that these spatial-coding cells form distinct clusters, with some cells being sensitive to external sensory changes while others remained stable. This underscores the complexity of sensory integration in spatial navigation and the distinct strategies employed by MEC in processing external sensory information. Moreover, whisker stimulation reliably induced responses in MEC cells, some of which exhibited spatial-coding properties during free exploration. These findings enhance our understanding of the role of whisker sensation in the MEC and its contribution to spatial computation during navigation.

All known types of spatial-coding cells are modulated to varying degrees by sensory information, with HD cells being particularly sensitive. For instance, HD cells in the subiculum respond to environmental rotation[37]. In blind mice, HD cells in the anterior dorsal nucleus (ADN) use olfactory cues to encode head direction[38]. Moreover, disruption of vestibular input impaired the head direction tuning in the anterior thalamus [39], leading to subsequent effects on the place cells in the hippocampus[40]. Our results showed that the MVL and HD tuning in the MEC decreased following the deprivation of visual and whisker-supported tactile inputs (Figures 1E-P; Figure S3J). The disruption of HD tuning caused by light deprivation could be explained by the known indirect and direct projections between MEC and the visual cortex[41,42] and the proven ability of HD cells to establish HD tuning by visual cues[32,43]. The novel influence observed following whisker trimming is particularly noteworthy. In rodents, whisker activity is closely linked to head movements, with the right-left asymmetry of whisker positioning preceding head movement[44], enabling obstacle detection and direction determination. Furthermore, head turns and eye movements are often coordinated, allowing animals to effectively integrate visual and tactile information[44,45]. Thus, it is plausible that animals rely on the integration of multiple sensory inputs to construct an accurate spatial map and some HD cells persistently updating their tuning according to continuous visual and tactile inputs.

Border cells, another crucial type of spatial-coding cell, are also significantly impacted by light deprivation and whisker trimming (Figures 3A-F; Figures S5H-J). Animals probably rely on vision to gauge distances from the boundaries. However, direct contact with walls via whiskers likely enables border cells to refine their firing fields with greater precision. Previous research has shown that rodents can use their whiskers to assess aperture widths with an accuracy finer than 5 mm[46]. Additionally, blind rats rely heavily on whisker input for gap-crossing and it is also true for sighted rats in darkness[27]. A possible explanation for our findings is that in darkness, the precision of the animals' distance judgment diminishes, and whisker trimming further exacerbates this deficiency.

Grid cells and speed cells exhibit consistent behavior, with their coding of position and velocity being severely disrupted in the dark[20] (Figure 4 and Figure 5), consistent with previous reports[20]. Further deprivation of whisker-provided tactile input did not deteriorate the spatial-coding of grid at population level and speed coding of speed cells. Even in the "sensory-sensitive grid cells" and "sensory-sensitive speed cells", change of most cells occurred immediately after light-deprivation rather than whisker trimming (Figures 4P and 5J). The difference in their performance from those of "sensory-resistant" cells also occurred mainly between the light and dark condition (Figures 4M-N and 5H-I). These results suggest that grid and speed cells tend to be regulated by visual rather than tactile inputs.

Previous research found that altering the environment's shape resulted in similar responses in MEC grid and speed cells, while HD cells responded differently[19]. Additionally, optogenetic stimulation of MEC L2 pyramidal cells revealed that only a subset of HD cells exhibited changes in firing rates similar to those observed in grid cells[47], which suggests that other HD cells may not belong to the same microcircuit involved in the continuous attractor network (CAN) [48]. Anatomical studies further indicated that grid cells cluster separately from HD and border cells, potentially functioning independently[49]. In our study, MEC HD and border cells exhibited distinct responses from grid and speed cells, consistent with these findings. Notably, conjunctive Grid × HD cells showed sensory dependencies similar to grid cells (Figure S4G-J), suggesting a closer functional integration with grid cells and the potential to provide both head direction and positional information to the attractor network. In contrast, pure HD cells may fulfill different roles.

Facial whiskers are vital sensory organs for nocturnal rodents like mice and rats, providing essential tactile inputs. The active movement of whiskers, known as whisking[50], facilitates environmental exploration and triggers sparse neuronal activity patterns in the primary somatosensory cortex (S1)[51]. However, the connection between the MEC and S1 is not well-studied. A Recent anterograde tracing studies indicate S1 projects to various brain regions, including the entorhinal area[52], though direct anatomical evidence linking S1 and MEC is still lacking. Our findings show that the activity of certain MEC neurons correlates with whisker movement (Figure 6 and Figure S12). This highlights a potential research direction, that is, the mechanisms by which S1 transmits whisker-related information to MEC. Combined with the observed impact of whisker trimming on spatial cell tuning, this implies that S1 may play a role in spatial navigation. Emerging evidence suggests the vibrissal system significantly influences hippocampal function and spatial navigation. Whisker deflection-evoked responses observed in hippocampal CA1 imply that tactile inputs are transmitted to this area via the somatosensory cortex, contributing to experience-dependent learning[53]. Permanent whisker removal reduces hippocampal neurogenesis and impairs spatial memory[54]. The hippocampal CA2 region responds to whisker stimulation, likely aiding the update of spatial cognitive map[24]. Additionally, place fields are modulated by tactile inputs and can be disrupted by whisker pad inactivation[5]. Given the strong hippocampus-MEC connectivity, these findings suggest a potential neural

circuit linking S1 and MEC. Notably, the claustrum (Cla) provides the MEC with multisensory information, including information from the primary motor cortex (M1), primary visual cortex (V1), and S1, thereby influencing its spatial-coding process[55]. This suggests that the Cla may serve as a relay, transmitting whisker-related information from S1 to the MEC, aiding in spatial map construction.

Previous studies on hippocampal place cells[5] and MEC grid and HD cells[20,56] have shown significant heterogeneity in cellular responses to sensory cues. In our study, HD cells were also categorized into distinct clusters (Figure 2). "Sensory-sensitive HD cells" adjusted their coding after light deprivation or whisker trimming, indicating a strong dependence on external sensory inputs, possibly integrating information from multiple sensory cortices. "Whisker-sensitive HD cells" likely rely on projections from the somatosensory cortex. In contrast, "sensory-resistant HD cells" were unaffected by sensory deprivation, possibly maintaining their tuning via vestibular inputs. Other spatial-coding cells also showed "sensitive" and "resistant" clusters, but no exclusive sensory-specific cluster was identified, suggesting a more integrated processing mannar or limitations in our methods.

These results suggest the MEC uses multiple mechanisms to process external sensory inputs such as visual and whisker-supported tactile inputs for spatial representation. "Sensory-resistant cells" maintain stable coding after initial map formation, providing a consistent spatial map that may become more robust with experience. On the other side, "sensory-sensitive cells" rapidly update the spatial map in response to external inputs, which help animals quickly respond to environmental change and construct new spatial maps for novel environment. This highlights the dynamic balance in MEC neural circuits between stability and adaptability, optimizing energy conservation while maintaining responsiveness to environmental changes. Future research should clarify the interconnections among different spatial-coding cell types, particularly identifying those that contribute to the formation of grid cells' hexagonal firing patterns. Additionally, it is crucial to determine how multisensory information is processed in the MEC—whether independently or in combination—and whether sensory-sensitive cell clusters form a distinct network in response to external sensory input.

Methods

Animal subjects

In this study, male C57BL/6 wild-type mice were used, with 13 allocated for the L-D-DW-LW experiment and 7 for whisker-related experiments, 4 of which were also included in the L-LW experiments. The Peking University Animal Use and Care Committee approved all procedures, which adhered to the guidelines set by the Association for Assessment and Accreditation of Laboratory Animal Care. The mice were individually housed under a 12-hour light/dark cycle at a temperature of 22°C, with unrestricted access to food and water. A running wheel was placed in the cage to enhance the mice's activity. Behavioral experiments were all conducted during the dark phase. All mice were 9 to 11 weeks old at the time of surgery and were 12 to 18 weeks old when the formal experiment was

conducted.

Surgery

The surgical protocol was refined based on previous research (Low et al., 2014)[57]. The mouse was placed in a glass chamber with isoflurane to be temporarily anesthetized and then fixed at a stereotactic frame and was continuously anesthetized by inhaling isoflurane through a mask with 1.2% isoflurane flowing at 0.2 L/min. During the experiment, mouse was treated with an eye cream of erythromycin to prevent vision damage. An appropriate portion of scalp was resected to expose the skull's dorsal surface and the tissue on the surface was cleaned up. A rectangle craniotomy measuring 2.0 mm in length and 1.4 mm in width was created over the right hemisphere, whose proximal edge centered 2.7 mm lateral to the midline and the distal edge was 4.0 mm away. The muscle near the craniotomy was carefully detached from the skull by surgery scissors. 200 nL of rAAV-hSyn-GCaMP6f-WPRE-hGh polyA/ AAV-hSyn-GCaMP6s-WPRE-hGh polyA was injected at a rate of 100 nL/min using a glass capillary (NANOLITER2020 Injector, World Precision Instruments, FL, USA), 3.1 mm lateral to the midline, 0.3 mm anterior to the superior margin of the transverse sinus and at a depth of 1.7 mm below the brain surface. The capillary was left in place for 10 minutes to let virus spread. Similarly, another 200 nL virus was injected 3.7 mm lateral to the midline, 0.3 mm anterior to the transverse sinus, and at a depth of 1.5 mm below the brain surface.

The interface of the brain and the cerebellum was found and a proper “pocket” between the brain and the cerebellum was created by a surgical forceps while the cortical dura remained intact. A prism with its custom-made holder was connected to a stereotactic micromanipulator (1760, Kopf, CA, USA) and tilted 10 degrees laterally to ensure the image surface of the prism was parallel to the brain's dorsal surface. The prism assembly, consisting of a customized 1 mm diameter GRIN (gradient-index) lens attached to a 1 mm square prism (Grintech, Germany), was slowly inserted to the previously made “pocket” (subdural space within the transverse fissure). During implantation, the prism assembly was slowly lowered and moved in the anterior direction until the imaging plane of the prism was flush against the brain. Kwik-cast (World Precision Instruments, FL, USA) was used to seal the junction of the prism and exposed brain tissue. The scalp and the skull were adhered together through tissue adhesive (3M, MN, USA). Then, dental cement was used to cover the full skull and a headbar was firmly sticked.

Experiment

Training process

After recovering from surgery, the mice were kept in starvation, maintained at 80~90％ of their normal body weight and given adequate water. The experimental arena was an 80 × 80 cm^2 white floor box, with three cue cards pasted on the three walls of the box. A camera was placed above the open-field to track animal’s movement and two LED were used to emit either a white light or red light. Before the formal experiment, mice were trained to get

familiar with the experimental environment for about one week. During the first adaptation stage, the mice freely ran in the open-field with no burden on the head, the experimenter stood outside and randomly sprinkled cookie crumbs into the arena to attract mice to forage for food. After mice were accustomed to persistently running in the box and had a good trajectory coverage, the training moved to the next stage. During this stage, the mice ran in the box with the optical fiber connected to its baseplate on the head and a helium balloon was attached to the fiber in an appropriate place to balance the weight. After they got used to run with the fiber and gained good performance, the formal experiment began.

Open-field experiments

Calcium imaging was performed with the miniature two-photon microscope[30] (LFMTPM-V2.0.1, Resolution: ~1 mm; working distance: ~1 mm, NA: 0.45 mm). Before imaging, the cover of the GRIN lens on the prism were removed, the gel was added to cover the surface of lens and then microscope was placed into the baseplate and locked with screws. GCaMP6f/GCaMP6s was excited at 920 nm, with the laser intensity ranging from 30 to 80 mW at the sample. Image acquisition was managed using GINKGO-MTPM (Transcend Vivoscope Biotech Co., Ltd, China). Images of 600 pixel × 512 pixel were captured at a resolution of ~0.89 μm/pixel and a frequency of 9–9.5 Hz with a femtosecond fiber laser (TVS-FL-01, Transcend Vivoscope Biotech Co., Ltd, China). Running trajectory was recorded through the camera on the ceiling at 25 Hz, behavioral videos and calcium imaging videos were simultaneously acquired by software GINKGO-MTPM (Transcend Vivoscope Biotech Co., Ltd, China).

Four-session task (L-D-DW-LW)

The formal Light-Dark-Dark, Whisker-trimmed-Light,Whisker-trimmed (L-D-DW-LW) was conducted continuously within one day. In the first session (L), neuron activity was recorded as the mouse freely explored the open field with the warm-light LED on, to establish a baseline performance. In the second session (D), the light was turned off to create a dark environment, testing the influence of visual input. After completing dark session, the mouse was head-fixed, and the experimenter quickly removed all its whiskers using scissors. The whisker-trimmed mouse was then placed back into its home cage to acclimate for a while before the subsequent experiments began. Once the mouse resumed normal activities (e.g., running on the wheel), it was then reintroduced into the open field for the third session (DW) exploration, where the light remained off, and tactile input mediated by whiskers was deprived. In the fourth session (LW), the light was turned on again to test whether the regained visual input could restore spatial cognition while tactile input was deprived. Each session lasted 25 to 40 minutes to ensure that the trajectory evenly covered the whole open field. Mice rested in their home cage for 5 minutes and received water between each session. Before formal recording, mice were placed in the open field to adapt. Data collected from 13 mice was used to further analysis.

Two-session task (L-LW)

To directly assess the impact of whisker trimming under light conditions, we conducted an additional Light-Light, Whisker-trimmed (L-LW) task using 4 mice. In this task, spatial-coding cells were allowed to establish their initial firing patterns during the baseline light session (L), followed immediately by whisker trimming.

Whisker-related experiment

For “stimulated-whisking” sessions, mice were fixed in a platform, the movement of whiskers were recorded through a camera directly above the mice’ head at about 45 Hz and neuron activity were simultaneously recorded by two-photon calcium imaging. A self-made automatic stimulator was placed on the side of the mouse's cheek to enhance their whisker movement, which contained an automatic telescopic rod with a piece of sandpaper at the end. A “stimulated-whisking” session contained 20 continuous trials, each trial lasted for 1 minute, consisting of 5 seconds of stimulation and 55 seconds of non-stimulation. During stimulation period, the rod was extended so that the sandpaper sheet at the end could be detected by most of the mice' whiskers and the mice showed a higher frequency of whisker movement (see Video S2). During the remaining non-stimulation period, the rod was in its retracted state and the whiskers had no contact with the sandpaper (see Video S1).

For “spontaneous-whisking” sessions, everything was the same as the “stimulated-whisking” session, except that no stimulus was presented to the mice, that is, the rod was always in its retracted state and no piece of sandpaper sheet could be accessed by whiskers. Mice showed less whisker movement in this session.

Histology

After completing all the experiments, the animals were anesthetized with isoflurane and then perfused with saline followed by 4% paraformaldehyde (PFA). Skin and muscles were removed from the skull cap with surgical scissors. The skull cap was fixed in PFA for at least 24 hours, to allow for fixation of the brain and cerebellum with the implant site of prism undeformed. The brain was cryoprotected in a 30% sucrose solution for 24 hours the day before slicing and the remaining skull cap and the prism were carefully removed. Sagittal sections of 30 μm thickness were obtained using a cryostat (Leica).

The brain slices were stained with DAPI, and for some mice, anti-GFP staining was also performed. For GFP staining, brain slices in PBS were first washed with a solution containing 10% goat serum and 0.3% TX100 in PBS for 1 h. They were then incubated overnight with the primary antibody (anti-GFP chicken, Thermo Fisher Scientific, catalog # A-10262, RRID AB_2534023, diluted 1:1000 in the goat serum/TX100/PBS solution) at 4℃. After this, the slices were washed again with the PBS for three 5-minute intervals before being incubated with the secondary antibody (goat anti-chicken IgY (H+L) Alexa Fluor 488, Thermo Fisher Scientific, catalog # A-11039, RRID AB_2534096, diluted 1:1000 in in the goat serum/TX100/PBS solution) at room temperature for two hours. Finally, the slices were washed twice for 5 minutes each in PBS at room temperature and then

mounted with DAPI (Sigma Aldrich, catalog # D9542). The stained sections and prism implantation position were visualized using an Olympus VS120 virtual slide microscope or Zeiss Axio Scan Z1. Images were further processed by ZEN microscope software (Carl Zeiss, Jena, Germany) and ImageJ (National Institutes of Health, Bethesda, MD, USA).

Data analysis

Behavioral videos were analyzed by DeepLabCut[58], which yielded the six points of body the animal in each frame: nose, left ear, right ear, head, body center and tail base.

Calcium imaging data processing for open-field experiments and whisker experiments were both conducted using the Python implementation of Suite2P[59]. Imaging views of continuous 3 or 4 sessions were carefully checked and then were registered together using Suite2P to perform cell detection and signal extraction. Subsequent processing of fluorescence signals was completed by MATLAB scripts adapted from the previous work by Zong et al[60].

For open-field experiments, the 80 × 80 cm^2 square was divided into 2.5 × 2.5 cm^2 bins to create spatial tuning maps, which represent neuron's calcium activity normalized by occupancy. Each bin's value in the tuning map was calculated as the ratio of the total calcium events to the duration spent in that bin. A Gaussian filter was applied to smooth position data. Arena coverage was defined as the proportion of visited bins to the total number of bins, with a bin considered visited if the animal spent at least 0.1 seconds there. To eliminate the effects of behavioral state changes (e.g., foraging versus resting), data points with running speeds below 2.5 cm/s or above 60 cm/s were excluded from all analyses of both observed and shuffled data.

Head-direction tuning maps and speed tuning curves were developed using similar methods (Range: 0-360° for head direction tuning curve and 2.5 cm/s – 18.5 cm/s for speed tuning function; bin size: 3° for head direction tuning curve, and 2 cm/s for speed tuning function). These values were then smoothed using a Gaussian filter (standard deviation: 2.5 cm for spatial heatmaps, 2° for head direction tuning curve, and 2 cm/s for speed tuning function).

Spatial information content, measured in bits per event, was determined using the formula[61]:

$$\sum_i p_i \frac{\lambda_i}{\lambda} log_2 \frac{\lambda_i}{\lambda}$$

where λ_i is the mean amplitude of calcium activity in the *i*-th location bin, λ is the overall mean amplitude, and p_i is the probability of the animal being in the *i*-th bin. Head information is calculated using the same method, except that p_i in this case is the probability of the animal's head direction being in the *i*-th angle bin.

Grid cells

All grid cells were selected from the baseline light session and assigned a grid score based on their autocorrelogram, as described by Sargolini et al.[14] Briefly, each cell's autocorrelogram was rotated at multiple angles, and Pearson correlations were calculated for rotations at 60° and 120° (Group 1) and at 30°, 90°, and 150° (Group-2). The minimum difference between any element in Group 1 and any element in Group 2 was determined. The grid score for each cell was defined as the highest minimum difference between Group 1 and Group 2 rotations across all successive circular samples. The central peak was not included in the analysis.

A cell was classified as a grid cell if its grid score exceeded a chance level determined by shuffling the experimental data 1,000 times. For each shuffle, the deconvolved calcium activity sequence of the cell was time-shifted along the animal's path by a random interval, following methods from Zong et al.[60] Additionally, for each cell, we recalculated the spatial tuning map for the first and second halves of the baseline session and computed the correlation between these two maps to assess intra-session stability. A cell was defined as a grid cell if its recorded grid score exceeded the 95th percentile of grid scores from the shuffled data and its intra-session stability was greater than 0.3 in baseline session.

For detailed analysis of grid cells' geometric features, we examined grid spacing and calculated ellipticity for each grid cell under each experimental conditional. Grid spacing was determined by measuring the distance from the center of each autocorrelogram to its six surrounding autocorrelation nodes, then averaging these distances. The standard deviation of these grid spacing values was calculated to reflect the regularity of grid pattern. To calculate ellipticity, an ellipse was fitted to the identified maxima using a least-squares method[62]. For cells where the fitting was successful, ellipticity (ε) was defined as the ratio of the semi-major (α) to semi-minor (β) axes of the fitted ellipse, yielding a value between 1 (a perfect circle) and infinity (∞). Only grid cells with an ellipticity value less than 5 in the baseline light session were included in the ellipticity-related analysis.

Position Decoding

Animal's position was decoded through a Naïve Bayes decoder[63] based on neural activity in a certain session. We modeled events from different cells as independent Poisson processes. Calcium event data was reassigned into intervals of 1 s and smoothed using a 5 s time window. The average position of the animal across all frames within each time window was used to represent the mouse's position in that specific time bin. For each time bin, the probability of the animal being in a specific position bin was calculated using the formula:

$$P(X|n) = CP(X)\left(\prod_{i=1}^{N} f_i(X)^{n_i}\right) e^{-\tau \sum_{i=1}^{N} f_i(X)}$$

where X is the spatial bin, the element n_i of vector $\mathbf{n} = (n_1, n_2, \ldots, n_N)$ is the number of calcium events for neuron i within each time bin, is a normalization factor, $P(X)$ indicates the overall probability of the animal occupying spatial bin X, $f_i(X)$ is the mean event rate

of cell i in spatial bin X, and τ is the length of the time window. While the vector n referred to testing data, other variables were derived from training data. The position with the maximum likelihood was identified as the animal's decoded position for each time bin. The decoding error for test data was calculated as the mean absolute error (MAE) between the actual position and the decoded position.

For each mouse with n grid cells, we randomly selected k cells from the total grid cells for k ranging from 1 to n to establish decoder for baseline session. This process was repeated 100 times to obtain the MAE of the decoder with k cells. We observed that the MAE gradually decreased as k increased, indicating an improvement in the decoder's performance (Figure S6D). Ultimately, we selected four mice with more than 20 grid cells each for subsequent statistical analysis related to decoding.

The first half of the baseline light session served as the training set, while the second half was used as the test set to establish a basic spatial-coding pattern when no sensory inputs were deprived. Subsequently, we decoded the animal's position using the second half of the following sessions (D, DW, LW) as the test set, based on the initial training set in baseline session, to investigate whether the spatial-coding pattern of grid cells changed after multi-sensory deprivation. A shuffled data set was created by randomly time-shifting the animal's position in the baseline light session for 1,000 times.

Border cells

The border score was calculated to assess the spatial firing patterns of cells in relation to the environment's boundaries, based on previously described methods[16], with adjustments for calcium imaging data. Fields of a cell were identified using a threshold set at 30% of the maximum firing rate within the map. The border score was then determined by calculating the difference between the highest coverage of any single field along any of the four walls and the average distance to the nearest wall for that field, weighted by event rate and normalized by half the shortest side of the environment. Border scores ranged from -1 to +1, with a score of +1 indicating cells with infinitely narrow fields perfectly aligned along the entire wall.

Border cells were identified based on their border scores significantly surpassing chance levels determined by a shuffling procedure, similar to that used for grid cells. A cell was classified as a border cell if its true border score exceeded the 95th percentile of scores from 1000 shuffled permutations of the same cell and the spatial correlation between the first and second halves of the baseline session was above 0.3.

Spatial cells

Spatial cells were characterized by a spatial correlation greater than 0.5 between the two halves of the baseline light session and spatial information content exceeding the 99th percentile of the shuffle distribution, excluding grid cells and border cells.

Speed cells

The method for calculating speed scores was adapted for calcium imaging data based on previous research (Method 1). Each session was divided into 1-second bins, and for each bin, the event rate and the mean running speed of the animals were calculated. The speed score for each cell was defined as the Pearson correlation between the series of event rates and the series of running speeds, ranging from −1 to 1. To establish chance-level statistics, a shuffling procedure was repeated 1,000 times, time-shifting the entire sequence of spikes relative to the animal's speed sequence for each repetition. A cell with a speed score exceeding the 99th percentile of the shuffled data was considered a speed cell candidate.

Speed tuning was analyzed over a range from 2.5 cm/s to 18.5 cm/s with a bin size of 2 cm/s. At each time point, the corresponding running speed and spike data were binned into predefined speed bins. The occupancy time for each bin was converted from frames to seconds, and event rates were calculated by dividing the spike count by the occupancy time in each speed bin. Bins with occupancy less than the minimum span time were excluded to ensure robustness. Besides, speed tuning was calculated separately for the first and second halves of the session, and intra-session stability was defined as the Pearson correlation between the two vectors. A cell was defined as a speed cell if its speed score exceeded the 99th percentile of the shuffled data (Method 1) and its intra-session stability was greater than 0.5.

Additionally, we developed another method (Method 2) to validate the reliability of Method 1. In this approach, the speed score was directly defined as the Pearson correlation between the mean event rate and mean running speed of each speed bin based on the previously acquired speed tuning. A cell was considered a speed cell only if it met both the score and intra-session stability thresholds, identical to those in Method 1. The speed cells identified by Method 2 overlapped by 70.0% with those identified by Method 1, yielding highly consistent statistical results in our analyses.

Head direction cells

All HD cells were selected from the baseline light session. We calculated the mean resultant vector (mean vector length, MVL) from the head direction tuning curve following the method described by Sargolini et al[14]. A cell was considered to be modulated by head direction if its MVL exceeded a chance level established by repeatedly shuffling the experimental data for 1,000 times. For each time, the deconvolved calcium activity sequence was randomly time-shifted relative to the sequence of head-direction of the mice. We also assessed the intra-session tuning stability of HD cell candidates by calculating the Pearson correlation between the head direction tuning curves from the first and second halves of the session. A cell was identified as a HD cell if its MVL was larger than the 99th percentile of MVLs from its shuffled data and had an intra-session stability larger than 0.5. Head information was calculated as described above to measure the information about animals' head direction conveyed by a HD cell. If a cell met the criteria for both HD cells and grid cells, it was classified as a Grid × HD cell; otherwise, it was categorized as a pure

HD cell.

Population vector (PV) correlation

To assess the change of populational coding of HD cells after sensory deprivation, we computed the population vector correlation between session pairs. The head direction was first divided into 120 angle bins (3° each). For each bin, we calculated the corresponding population vector (PV) by concatenating the mean event rates of all HD cells associated with that bin. Subsequently, the Pearson correlation between PV for every possible pair of angular bins was calculated for each mouse, resulting in a correlation matrix for each session. Each value within this matrix represents the correlation between the PV of two specific angular bins. We then computed the mean correlation across all mice for each bin pair, yielding an averaged correlation matrix for each session pair. These averaged matrices were then combined into a single comprehensive matrix, which provides a visual representation of the consistency in head direction tuning across different sessions and angular bins (Figure 1K). Additionally, we compiled the tuning curves of all HD cells into a 2-dimensional matrix for each mouse, referred to as the population vector matrix. The correlation between these PV matrices was computed across session pairs. The mean and SEM of the PV correlations for all mice (n = 13) are presented in Figure 1L, with color representing the correlation values.

For both border cells, grid cells and spatial cells (Figures 3J,4O and S11I-J), the PV matrix correlation of each cluster was calculated individually to illustrate the differences after sensory deprivation. We rearranged the 2D rate map of each cell (sized 33 × 33) into a 1D row vector (sized 1 × 1089) and combined the event rates from all cells within a cluster. This resulted in a 2D population vector matrix for each mouse in each session. We subsequently computed the PV matrix correlation between session pairs for each mouse and each cluster. By averaging these data across all mice, we assessed the changes in the populational coding of grid cells and border cells for each cluster after sensory deprivation.

Linear Mixed-effects Model

For comparisons involving neurons from multiple mice, we utilized linear mixed-effects (LME) models to account for the dependency of neuron properties on mouse identity. Specifically, when comparing cell scores across two sessions, we included the scores along with cell ID, session ID, and mouse ID in our analysis. The dataset was processed using the MATLAB function *fitlme*. In the model, the fixed-effects portion was attributed to session ID, while the random-effects portion was attributed to mouse ID and cell ID. This model provided a more accurate estimation of the effect of sessions on scores compared to ANOVA[31].

In our study, LME was utilized for statistical analyses of the population MVL and head information in all head direction cells (Figure 1F-G,I-J), border score and spatial information in border cells (Figure 3B-C,E-F), grid score and spatial information in grid cells (Figure

4B-C,E-F), speed score and tuning slope in speed cells (Figure 4B-C,E-F), and spatial information in spatial cells (Figure S11B,D).

Gaussian Mixture Model

A Gaussian Mixture Model (GMM) was employed to cluster spatial-coding cells based on their response to multisensory deprivation. For HD cells, the GMM utilized the correlation of HD tuning and ΔMVL between sessions L and D, and between sessions D and DW. For border cells, grid cells, and other spatial cells, spatial correlations between session pairs were used, while for speed cells, the correlation of speed tuning was employed. We tested cluster numbers ranging from 2 to 6. For each cluster number k, the GMM was performed 500 times, with silhouette analysis conducted each time to validate the clustering results. The maximum and mean silhouette coefficients from these 500 runs were used to determine the optimal number of clusters, identifying a local maximum at

k = 3 clusters for HD cells and k = 2 for other spatial coding cells. No outliers were excluded during the clustering process. To visualize the data, a principal component analysis (PCA) model was applied to the GMM outputs of HD cells, reducing the dimensionality to the first two principal components.

Additionally, the distribution of other variables not included in the GMM, such as the absolute change of preferred direction (ΔPFD) for HD cells, Δ Border score for border cells, and Δ stability for grid cells, were plotted. This was done to verify the clustering results and to identify which cell clusters were sensitive to external sensory inputs.

LDA-based dimensional reduction

To investigate the structure of head-direction representation and its alteration under sensory deprivation, we applied linear discriminant analysis (LDA)[64], a supervised dimensionality reduction technique. LDA seeks an optimal linear transformation that maximizes between-class variance while minimizing within-class variance. In our study, we used LDA-based method to project the high-dimensional neuronal activity on a 2-dimensional plane with best separation of head direction tuning.

First, we computed neural trajectories in an N-dimensional space using a binary matrix $A \in \mathbb{R}^{N\times T}$ to represent the calcium events, where N is the number of identified head-direction cells in the baseline session, and T is the number of time frames. Each matrix $A_{i,j}$, indicate the present (1) or absence (0) of a calcium event for neuron i at time j. We then divided the time frames into overlapping time bins, smoothing the data to reduce variance. Event rates of each neuron were calculated for each bin, and head-direction angles were assigned based on the direction nearest to the bin center, resulting in an N-dimensional neural trajectory matrix $B \in \mathbb{R}^{N\times T'}$and a corresponding head-direction array $H \in \mathbb{R}^{T'}$. These were then subjected to LDA for dimensionality reduction.

LDA calculates two scatter matrices, S_W(within-class) and S_B(between-class), and finds the optimal linear transformation Θ^* that maximizes the Fisher's linear discriminant ratio

$$J = \frac{|\Theta^{\mathrm{T}} S_B \Theta|}{|\Theta^{\mathrm{T}} S_W \Theta|}$$

We used data from the baseline light session to derive Θ^*, which was then applied to project neuron activity from subsequent sensory deprivation sessions.

Intuitively, the Fisher's linear discriminant ratio is an appropriate metric to assess the separability of data points in terms of their head directions. Additionally, we adopted the separation index

$$SI = \frac{\sum_{i=1}^{C} \sum_{j=i+1}^{C} \|u_i - u_j\|}{\sum_{i=1}^{C} \sum_{j \in C_i}^{C} \|B_{:,j} - u_i\|}$$

to cross-validate our findings on the deterioration of the separability of head directions caused by sensory deprivation.

Whisker-related analysis

Identification of "whisker-sensitive" cells

Videos recording whisker movement were analyzed by Facemap[65], which yielded the position of the start and middle points of a selected whisker in each frame, also named as root and tail points. The root and tail positions were determined by comparing the standard deviations of the initial position data, with the position set having a higher standard deviation designated as the tail, and the other as the root. The mean positions for both the root and tail points were calculated to establish the initial vector ($\vec{0}$) between these mean positions. For each frame, the vector ($\vec{\imath}$) between the root and tail positions was computed, and the angle (θ) between $\vec{0}$ and $\vec{\imath}$ was calculated. Following the angle calculation, the angles were smoothed using a Gaussian filter with a window size of 2s to obtain θ_{smooth}. The change in angle (θ_{change}) was then calculated as the difference between consecutive smoothed angles. For each time in the neuronal activity data, the corresponding time in the behavioral data was identified by finding the closest matching time point. The mean absolute values of θ_{change} over each interval between consecutive timestamps of calcium trace were then smoothed using a Gaussian filter with a window size of 1s to obtain the final value of whisker movement. The whisker movement sequences of three distinct whiskers from the same animal were highly similar, demonstrating the reliability of our method and suggesting that this whisker movement sequence can be effectively used in whisker-related neuronal activity studies.

A cell was considered "whisker-sensitive" if the Pearson correlation between its denoised ΔF/F sequence and the whisker movement sequence exceeded a chance level determined by shuffling the experimental data 1,000 times. For each shuffle, the deconvolved calcium activity sequence was randomly shifted relative to the whisker movement. The Pearson correlation of the shuffled denoised ΔF/F and its corresponding whisker movement sequence was recalculated to create a shuffle dataset. A cell was identified as "whisker-sensitive" if its true correlation exceeded the 95th percentile of correlations from the

shuffled data in the "stimulated-whisking" session.

Calcium imaging data collected from the "free-exploration" session, "spontaneous-whisking" session, and "stimulated-whisking" session were analyzed together using Suite2P to identify the same cells across these sessions and assign spatial-coding identities based on their performance in the "free-exploration" session. The standards used for cell detection were consistent with those used in open-field experiments.

Mutual information

Mutual information (MI) was calculated between the distributions of denoised ΔF/F and whisker movement values across individual frames. Whisker movement values were automatically divided into 10 ~ 12 bins with equal size after bins whose total values had an occupancy less than 150 frames were excluded (exclude proportion: mean ± SEM: 4.6％± 0.3％). The distribution of whisker movement was $P(X = x), x \in X$. Similarly, for each neuron's denoised ΔF/F, the variable Y, $P(Y = y)$ was determined after denoised ΔF/F values were automatically divided after bins with fewer than 100 observations were excluded, leading to an average bin number of 28.

After the joint distribution of whisker movement and neuronal activity $P(x, y)$ was estimated, MI [35] was then computed by summing the joint probabilities multiplied by the log ratio of joint probabilities to the product of marginal probabilities as follow.

$$MI(X;Y) = \sum_{x \in X, y \in Y} P(x, y) log_2 \frac{P(x,y)}{P(x)P(y)}$$

Here, $P(x, y)$ represents the joint probability of both variables occurring together, and $P(x)$ and $P(y)$ are the marginal probability of the whisker movement and denoised ΔF/F, respectively .

Additionally, the conditional probability of denoised ΔF/F given whisker movement were calculated and a linear regression was performed to determine the extent to which a neuron's firing was positively tuned by whisker movement.

Acknowledgments

This research was funded by the Qidong-SLS Innovation Fund (2023002029 and 2020001540; C.M.), the Space Brain Project of Lingang Laboratory (Grant No. LG-TKN-202204-01; C.M.), the Science Fund for Distinguished Young Scholars in Beijing (JQ23023; C.M.), the Chinese Government Foreign Expert Project for Emilio Kropff (G2022101003L; C.M.), and the PICT-2019-2596 grant from the Argentine Ministry of Science (E.K.). We are grateful to the National Center for Protein Sciences at Peking University in Beijing, China, for their support with imaging and histology. Thank Xiang Zhang and Meng Zhong for their invaluable guidance on experiment techniques and data processing during the early stages of this project.

Author contributions

C.M, J.T designed research, J.T collected the data, W.S, Y.Z, X.Z performed the surgery,

J.T, Y.Z, S.Y analyzed the data. C.M supervised the project, J.T, C.M. wrote the paper with input from all authors.

Declaration of interests

The authors declare no competing interests.

Supplementary information

Figures S1–S12. Videos S1-2.

References

1 Terry, A. V., Jr. in *Methods of Behavior Analysis in Neuroscience Frontiers in Neuroscience* (ed J. J. Buccafusco) (2009).

2 Rossier, J., Haeberli, C. & Schenk, F. Auditory cues support place navigation in rats when associated with a visual cue. *Behavioural Brain Research* **117**, 209–214 (2000).

3 Watanabe, S. & Yoshida, M. Auditory cued spatial learning in mice. *Physiol Behav* **92**, 906–910 (2007).

4 Bao, X. *et al.* Grid-like Neural Representations Support Olfactory Navigation of a Two-Dimensional Odor Space. *Neuron* **102**, 1066–1075 (2019).

5 Gener, T., Perez-Mendez, L. & Sanchez-Vives, M. V. Tactile modulation of hippocampal place fields. *Hippocampus* **23**, 1453–1462 (2013).

6 Mittelstaedt, M. L. & Mittelstaedt, H. Homing by Path Integration in a Mammal. *Naturwissenschaften* **67**, 566–567 (1980).

7 McNaughton, B. L. *et al.* Deciphering the hippocampal polyglot: The hippocampus as a path integration system. *J Exp Biol* **199**, 173–185 (1996).

8 Touretzky, D. S. & Redish, A. D. Theory of rodent navigation based on interacting representations of space. *Hippocampus* **6**, 247–270 (1996).

9 Seelig, J. D. & Jayaraman, V. Neural dynamics for landmark orientation and angular path integration. *Nature* **521**, 186–191 (2015).

10 Perez-Escobar, J. A., Kornienko, O., Latuske, P., Kohler, L. & Allen, K. Visual landmarks sharpen grid cell metric and confer context specificity to neurons of the medial entorhinal cortex. *Elife* **5**, doi:10.7554/eLife.16937 (2016).

11 Hardcastle, K., Ganguli, S. & Giocomo, L. M. Environmental Boundaries as an Error Correction Mechanism for Grid Cells. *Neuron* **86**, 827–839 (2015).

12 McNaughton, B. L., Battaglia, F. P., Jensen, O., Moser, E. I. & Moser, M. B. Path integration and the neural basis of the 'cognitive map'. *Nature reviews. Neuroscience* **7**, 663–678 (2006).

13 Hafting, T., Fyhn, M., Molden, S., Moser, M. B. & Moser, E. I. Microstructure of a spatial map in the entorhinal cortex. *Nature* **436**, 801–806 (2005).

14 Sargolini, F. *et al.* Conjunctive representation of position, direction, and velocity in entorhinal cortex. *Science* **312**, 758–762 (2006).

15 Savelli, F., Yoganarasimha, D. & Knierim, J. J. Influence of boundary removal on the spatial representations of the medial entorhinal cortex. *Hippocampus* **18**, 1270–1282 (2008).

16 Solstad, T., Boccara, C. N., Kropff, E., Moser, M. B. & Moser, E. I. Representation of Geometric Borders in the Entorhinal Cortex. *Science* **322**, 1865–1868 (2008).

17 Kropff, E., Carmichael, J. E., Moser, M. B. & Moser, E. I. Speed cells in the medial entorhinal cortex. *Nature* **523**, 419–424 (2015).

18 Hinman, J. R., Brandon, M. P., Climer, J. R., Chapman, G. W. & Hasselmo, M. E. Multiple Running Speed Signals in Medial Entorhinal Cortex. *Neuron* **91**, 666–679 (2016).

19 Munn, R. G. K., Mallory, C. S., Hardcastle, K., Chetkovich, D. M. & Giocomo, L. M. Entorhinal velocity signals reflect environmental geometry. *Nat Neurosci* **23**, 239–251 (2020).

20 Chen, G., Manson, D., Cacucci, F. & Wills, T. J. Absence of Visual Input Results in the Disruption of Grid Cell Firing in the Mouse. *Current biology : CB* **26**, 2335–2342 (2016).

21 Dannenberg, H., Lazaro, H., Nambiar, P., Hoyland, A. & Hasselmo, M. E. Effects of visual inputs on neural dynamics for coding of location and running speed in medial entorhinal cortex. *Elife* **9**, doi:10.7554/eLife.62500 (2020).

22 Adibi, M. Whisker-Mediated Touch System in Rodents: From Neuron to Behavior. *Front Syst Neurosci* **13**, 40 (2019).

23 Vincent, S. B. *The Functions of the Vibrissae in the Behavior of the White Rat*. Vol. 1 (University of Chicago, 1912).

24 Pereira, A. *et al.* Processing of tactile information by the hippocampus. *Proc Natl Acad Sci U S A* **104**, 18286–18291 (2007).

25 Knutsen, P. M., Pietr, M. & Ahissar, E. Haptic object localization in the vibrissal system: behavior and performance. *J Neurosci* **26**, 8451–8464 (2006).

26 Hutson, K. A. & Masterton, R. B. The sensory contribution of a single vibrissa's cortical barrel. *J Neurophysiol* **56**, 1196–1223 (1986).

27 Jenkinson, E. W. & Glickstein, M. Whiskers, barrels, and cortical efferent pathways in gap crossing by rats. *J Neurophysiol* **84**, 1781–1789 (2000).

28 Prigg, T., Goldreich, D., Carvell, G. E. & Simons, D. J. Texture discrimination and unit recordings in the rat whisker/barrel system. *Physiol Behav* **77**, 671-675 (2002).

29 Von Heimendahl, M., Itskov, P. M., Arabzadeh, E. & Diamond, M. E. Neuronal activity in rat barrel cortex underlying texture discrimination. *Plos Biology* **5**, 2696–2708 (2007).

30 Zong, W. J. *et al.* Miniature two-photon microscopy for enlarged field-of-view, multi-plane and long-term brain imaging. *Nature Methods* **18**, 46–49 (2021).

31 Yu, Z. X. *et al.* Beyond t test and ANOVA: applications of mixed-effects models for more rigorous statistical analysis in neuroscience research. *Neuron* **110**, 21–35 (2022).

32 Ajabi, Z., Keinath, A. T., Wei, X. X. & Brandon, M. P. Population dynamics of head-

direction neurons during drift and reorientation. *Nature* **615**, 892–899 (2023).

33 Fuhs, M. C. & Touretzky, D. S. A spin glass model of path integration in rat medial entorhinal cortex. *Journal of Neuroscience* **26**, 4266–4276 (2006).

34 Wallach, A., Bagdasarian, K. & Ahissar, E. On-going computation of whisking phase by mechanoreceptors. *Nat Neurosci* **19**, 487–493 (2016).

35 Cover, T. M. *Elements of information theory*. (John Wiley & Sons, 1999).

36 Moser, M. B., Rowland, D. C. & Moser, E. I. Place cells, grid cells, and memory. *Cold Spring Harb Perspect Biol* **7**, a021808 (2015).

37 Taube, J. S., Muller, R. U. & Ranck, J. B., Jr. Head-direction cells recorded from the postsubiculum in freely moving rats. I. Description and quantitative analysis. *J Neurosci* **10**, 420–435 (1990).

38 Asumbisa, K., Peyrache, A. & Trenholm, S. Flexible cue anchoring strategies enable stable head direction coding in both sighted and blind animals. *Nature communications* **13**, 5483 (2022).

39 Stackman, R. W. & Taube, J. S. Firing properties of head direction cells in the rat anterior thalamic nucleus: dependence on vestibular input. *J Neurosci* **17**, 4349–4358 (1997).

40 Stackman, R. W., Clark, A. S. & Taube, J. S. J. H. Hippocampal spatial representations require vestibular input. *Hippocampus* **12**, 291303 (2002).

41 Olsen, G. M., Ohara, S., Iijima, T. & Witter, M. P. Parahippocampal and retrosplenial connections of rat posterior parietal cortex. *Hippocampus* **27**, 335–358 (2017).

42 Shao, Q. *et al.* A non-canonical visual cortical-entorhinal pathway contributes to spatial navigation. *Nature communications* **15**, 4122 (2024).

43 Sit, K. K. & Goard, M. J. Coregistration of heading to visual cues in retrosplenial cortex. *Nature communications* **14**, 1992 (2023).

44 Towal, R. B. & Hartmann, M. J. Right-left asymmetries in the whisking behavior of rats anticipate head movements. *J Neurosci* **26**, 8838–8846 (2006).

45 Volle, M. & Guitton, D. Human gaze shifts in which head and eyes are not initially aligned. *Exp Brain Res* **94**, 463–470 (1993).

46 Krupa, D. J., Matell, M. S., Brisben, A. J., Oliveira, L. M. & Nicolelis, M. A. Behavioral properties of the trigeminal somatosensory system in rats performing whisker-dependent tactile discriminations. *J Neurosci* **21**, 5752–5763 (2001).

47 Zutshi, I. *et al.* Recurrent circuits within medial entorhinal cortex superficial layers support grid cell firing. *Nature communications* **9**, 3701 (2018).

48 Tukker, J. J. *et al.* Microcircuits for spatial coding in the medial entorhinal cortex. *Physiol Rev* **102**, 653–688 (2022).

49 Obenhaus, H. A. *et al.* Functional network topography of the medial entorhinal cortex. *Proceedings of the National Academy of Sciences of the United States of America* **119**, doi:ARTN e2121655119 (2022).

50 Welker, W. I. Analysis of sniffing of the albino rat. *Behaviour, Leiden* **22**, 223–244 (1964).

51 Crochet, S. & Petersen, C. C. H. Correlating whisker behavior with membrane

potential in barrel cortex of awake mice. *Nature Neuroscience* **9**, 608–610 (2006).

52 Liu, Y. *et al.* Cell class-specific long-range axonal projections of neurons in mouse whisker-related somatosensory cortices. *eLife* (in review, 2024).

53 Le Merre, P. *et al.* Reward-Based Learning Drives Rapid Sensory Signals in Medial Prefrontal Cortex and Dorsal Hippocampus Necessary for Goal-Directed Behavior. *Neuron* **97**, 83–91 (2018).

54 Gonzalez-Perez, O., López-Virgen, V. & Ibarra-Castaneda, N. Permanent Whisker Removal Reduces the Density of c-Fos+ Cells and the Expression of Calbindin Protein, Disrupts Hippocampal Neurogenesis and Affects Spatial-Memory-Related Tasks. *Front Cell Neurosci* **12**, 132 (2018).

55 Kitanishi, T. & Matsuo, N. Organization of the Claustrum-to-Entorhinal Cortical Connection in Mice. *J Neurosci* **37**, 269–280 (2017).

56 Kornienko, O., Latuske, P., Bassler, M., Kohler, L. & Allen, K. Non-rhythmic head-direction cells in the parahippocampal region are not constrained by attractor network dynamics. *eLife* **7**, doi:10.7554/eLife.35949 (2018).

57 Low, R. J., Gu, Y. & Tank, D. W. Cellular resolution optical access to brain regions in fissures: imaging medial prefrontal cortex and grid cells in entorhinal cortex. *Proc Natl Acad Sci U S A* **111**, 18739–18744 (2014).

58 Mathis, A. *et al.* DeepLabCut: markerless pose estimation of user-defined body parts with deep learning. *Nature Neuroscience* **21**, 1281–1291 (2018).

59 Pachitariu, M. *et al.* Suite2p: beyond 10,000 neurons with standard two-photon microscopy. *bioRxiv* 2016. DOI: https://doi.org/10.1101/061507.

60 Zong, W. J. *et al.* Large-scale two-photon calcium imaging in freely moving mice. *Cell* **185**, 1240–1256 (2022).

61 Skaggs, W., Mcnaughton, B. & Gothard, K. J. A. i. n. i. p. s. An information-theoretic approach to deciphering the hippocampal code. **5** (1992).

62 Fitzgibbon, A., Pilu, M., Fisher, R. B. J. I. T. o. p. a. & intelligence, m. Direct least square fitting of ellipses. **21**, 476–480 (1999).

63 Zhang, K., Ginzburg, I., McNaughton, B. L. & Sejnowski, T. J. Interpreting neuronal population activity by reconstruction: unified framework with application to hippocampal place cells. *J Neurophysiol* **79**, 1017–1044 (1998).

64 Li, C. & Wang, B. J. C. N. U. Fisher linear discriminant analysis. **6** (2014).

65 Syeda, A. *et al.* Facemap: a framework for modeling neural activity based on orofacial tracking. *Nat Neurosci* **27**, 187–195 (2024).

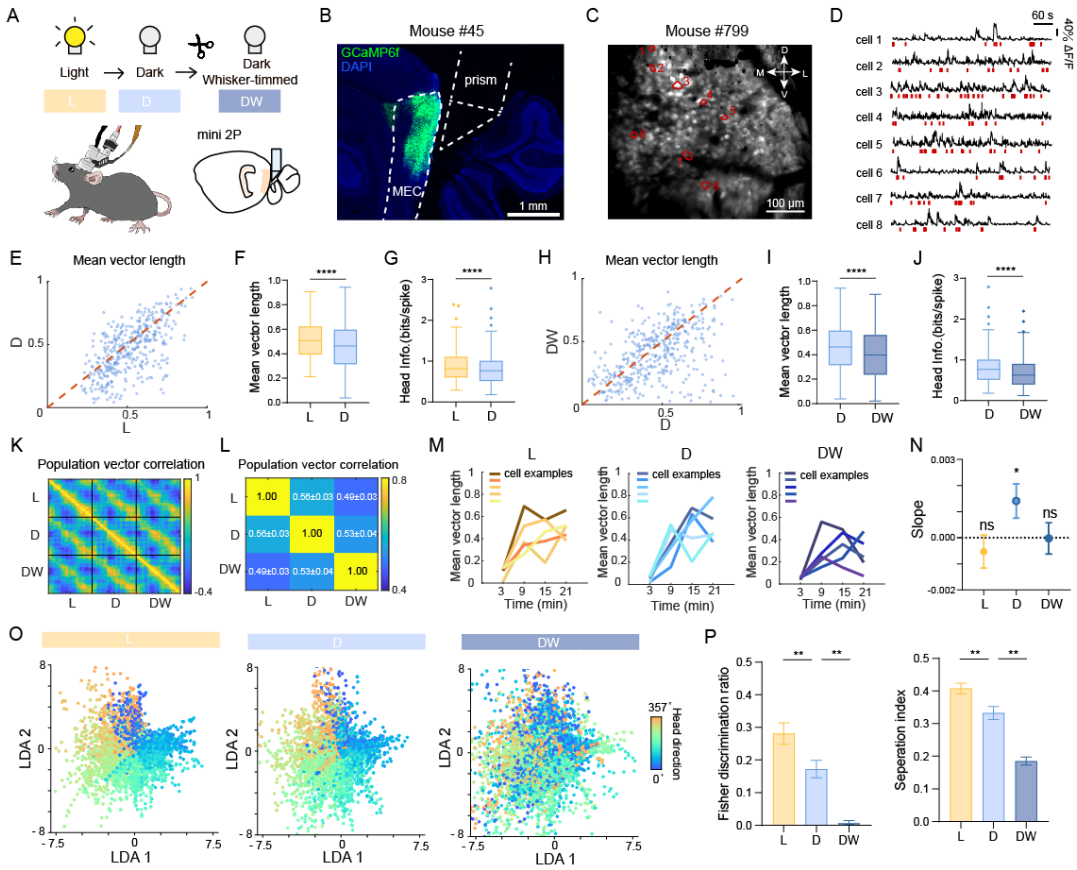

Figure 1. Two-photon imaging and changes in HD cell populations following light deprivation and whisker trimming.

(A) Schematic of the experimental setup, illustrating miniaturized two-photon recordings of MEC neuronal activity in freely moving mice under different conditions: Light (L), Dark (D), and Dark, Whisker-trimmed (DW).

(B) Representative histological image showing GCaMP6f expression in the MEC with a prism inserted at the cerebellar interface. Scale bar, 1 mm.

(C) Example field of view (FOV), with red outlines indicating example regions of interest (ROIs). The white coordinates denote the dorsal-ventral (D-V) and medial-lateral (M-L) axes of the FOV. Scale bar, 100 μm.

(D) Denoised ΔF/F calcium traces of several example neurons shown in (C).

(E) Scatter plot showing the distribution of MVL of all HD cells (n = 406) in Light (L) and Dark (D) conditions.

(F) Box plot showing the significant reduction in MVL of HD cells from L to D (two-sided t-test, $P = 1.8 \times 10^{-12}$, n = 406).

(G) Significant decrease in head information (bits/spike) from L to D (two-sided t-test, $P = 1.8 \times 10^{-12}$, n = 406).

(H-J) Similar analyses as in (E-G), showing changes in MVL and head information from Dark (D) to Dark, Whisker-trimmed (DW) (two-sided *t*-test, MVL: $P = 5.6 \times 10^{-6}$, Head Info.: $P = 9.3 \times 10^{-10}$, n = 406)

(K) Population vector correlation of HD cells across sessions, with 120 angular bins per

session. Color represents correlation values, with yellow indicating the highest and blue the lowest.

(L) Correlation between population vector matrices of all HD cells between each session pair, shown as mean ± SEM, n = 13 mice.

(M) Time course of MVL in HD cells under different experimental conditions, indicating a steady state in L, recovery in D, and no recovery in DW. Colorful lines represent five example cells with lowest initial MVL in each session.

(N) Statistical analysis of all the slopes derived from linear fits to MVL over time as shown in (M) , comparing slopes to zero using a one-sample *t*-test (L: n = 402, P = 0.41; D: n = 399, P = 0.0014; DW: n = 402, P = 0.97).

(O) LDA projections of HD cell activity in individual session along axes of maximal head direction separability, with colors representing different head directions.

(P) Fisher discrimination ratio and Separation index across sessions for each mouse, showing significant decreases after light deprivation (L/D) and whisker trimming (D/DW) (paired *t*-test, Fisher discrimination ratio: L/D: P = 3.9 × 10^{-6}, D/DW: P = 1.8 × 10^{-4}; Separation index: L/D: P = 5.9 × 10^{-4}, D/DW: P = 4.5 × 10^{-5}, n = 9 mice).

****P ≤ 0.0001; ***P ≤ 0.001; **P ≤ 0.01; *P ≤ 0.05; ns, P > 0.05.

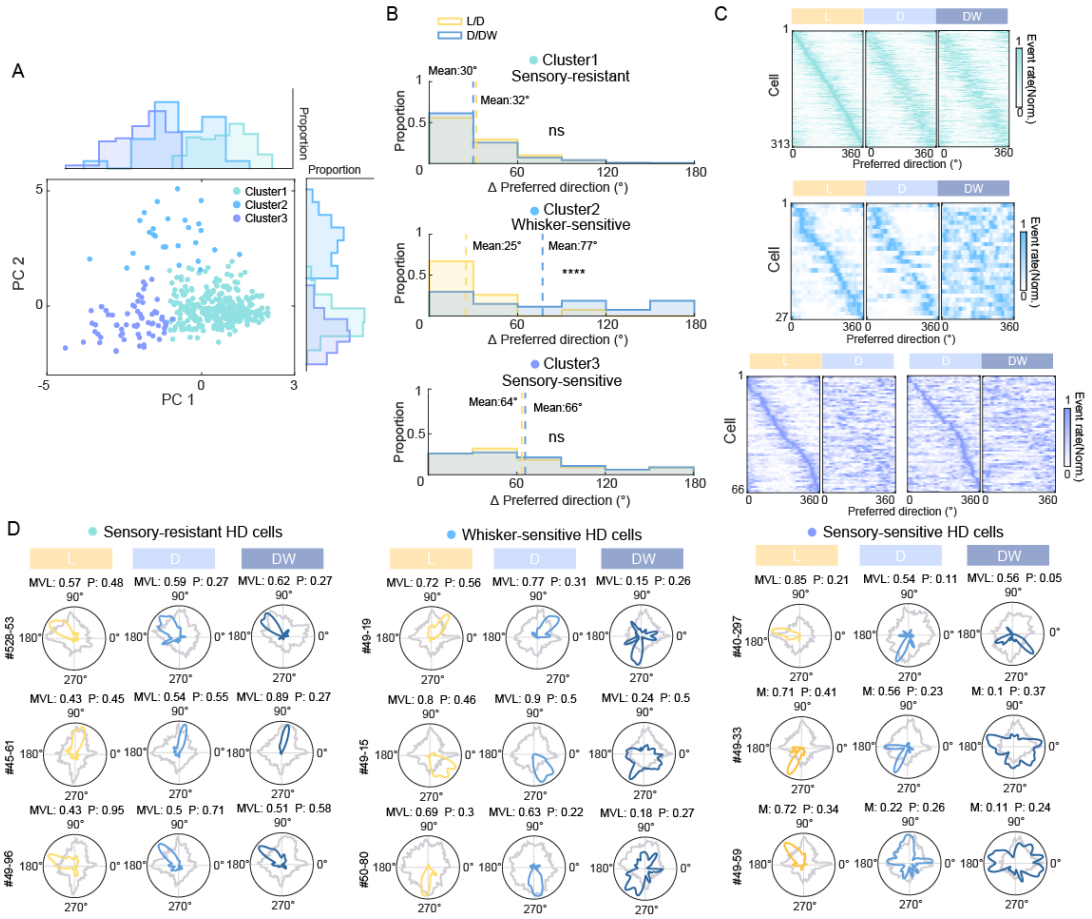

Figure 2. Differential responses of MEC HD cell clusters to visual and whisker-supported tactile deprivation.

(A) Gaussian Mixture Model (GMM) clusters HD cells (n = 406) into three distinct clusters,

displayed in a two-dimensional space defined by the first two principal components (PC1 and PC2).

(B) Sensitivity of distinct HD cell clusters to external sensory changes, illustrated by the distribution of changes in preferred direction (ΔPFD). Cluster 1 (sensory-resistant) exhibited minimal changes in ΔPFD under both light deprivation (L/D: mean ΔPFD = 32°) and whisker trimming conditions (D/DW: mean ΔPFD = 32°; KS-test, n = 313, P = 0.19). Cluster 2 (whisker-sensitive) showed significant changes in HD tuning after whisker trimming (L/D: mean ΔPFD = 25°; D/DW: mean ΔPFD = 77°; KS-test, n = 27, P = 7.7 × 10^{-4}). Cluster 3 (sensory-sensitive) displayed substantial changes in response to both visual and tactile input alterations (L/D: mean ΔPFD = 64°; D/DW: mean ΔPFD = 66°; KS-test, n = 66, P = 0.99).

(C) Populational tuning curves across experimental conditions for each HD cell cluster. Cells in Cluster 1 and Cluster 2 are sorted by their PFD in the baseline session (L). For Cluster 3, the first two columns are sorted by PFD in the baseline session (L), and the last two columns are sorted by PFD in the dark session (D).

(D) Representative examples of tuning curves across sessions for different HD cell clusters. ****P ≤ 0.0001; ***P ≤ 0.001; **P ≤ 0.01; *P ≤ 0.05; ns, P > 0.05.

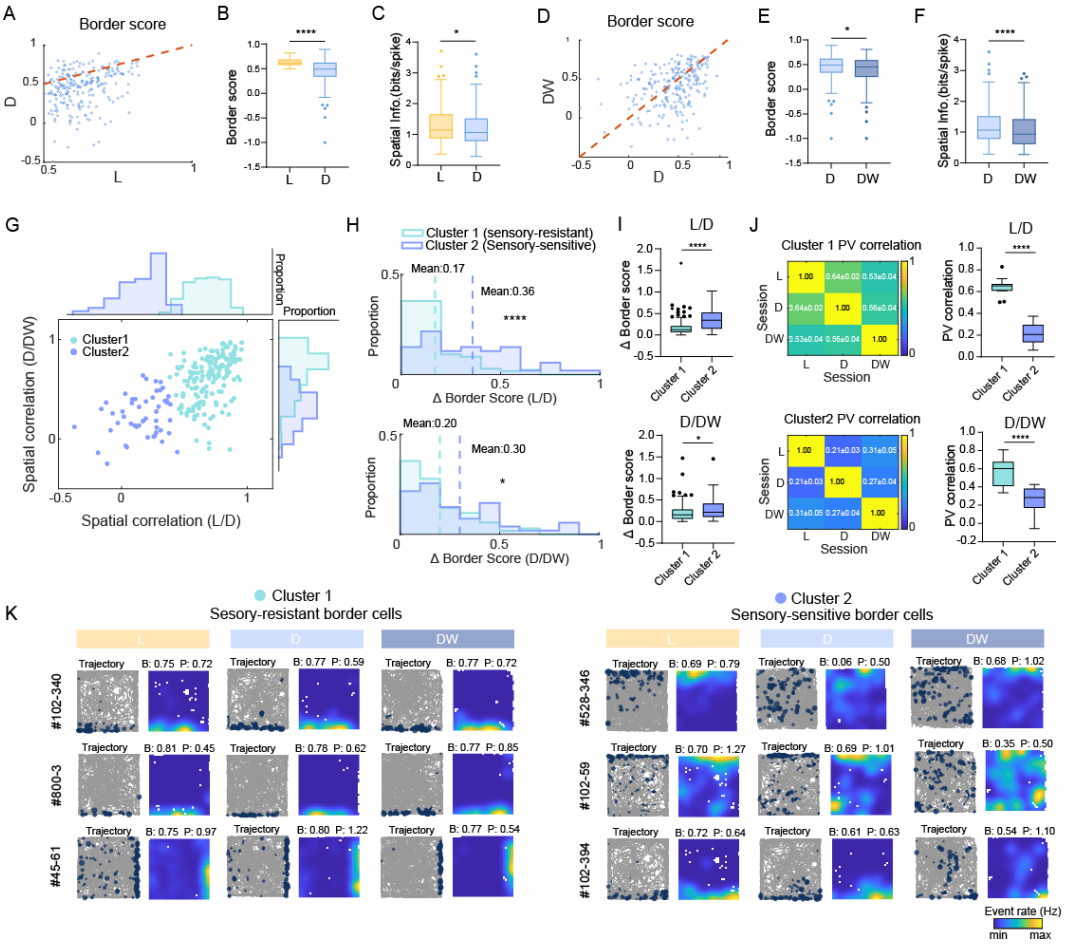

Figure 3. MEC border cells are modulated by both visual and whisker-supported tactile inputs.

(A) Scatter plot illustrating the distribution of border score for all border cells (n = 220) in Light (L) and Dark (D) conditions.

(B) Box plot showing a significant reduction in border score from L to D (two-sided *t*-test, $P = 2.8 \times 10^{-25}$, n = 220).

(C) Box plot demonstrating a significant decrease in spatial information (bits/spike) from L to D (two-sided *t*-test, P = 0.04, n = 220).

(D-F) Similar analyses as shown in (A-C), depicting changes in border scores and spatial information after whisker trimming (D/DW) (two-sided *t*-test, border score: P = 0.02; spatial information: $P = 4.4 \times 10^{-5}$, n = 220).

(G) GMM clustering identifies two distinct clusters of border cells based on spatial correlation of their rate maps across session pairs. Cluster 1 exhibits higher spatial correlation between L/D and D/DW sessions, whereas Cluster 2 shows lower spatial correlation.

(H) Histograms of Δ Border score for different cell clusters, indicating that Cluster 1 (sensory-resistant) has a smaller Δ Border score compared to Cluster 2 (sensory-sensitive) during both L/D (KS-test, n = 169 and n = 51, $P = 1.7 \times 10^{-7}$) and D/DW (KS- test, P = 0.03).

(I) Statistical comparison of Δ Border score for the two clusters between experimental conditions, revealing significant differences between Cluster 1 and Cluster 2 (L/D: Welch's *t*-test, n = 169 and n = 51, $P = 3.9 \times 10^{-6}$; D/DW: P = 0.02).

(J) Right: Correlation of population vector matrices for different border cell clusters across sessions, with color-coded bins representing correlation values (yellow: high correlation, blue: low correlation). Left: Box plots show that Cluster 1 demonstrates higher correlations following sensory deprivation compared to Cluster 2. (paired *t*-test, n = 12, L/D: $P = 4.0 \times 10^{-7}$; D/DW: $P = 2.9 \times 10^{-5}$)

(K) Representative spatial rate maps for border cells from Cluster 1 (sensory-resistant) and Cluster 2 (sensory-sensitive) across different experimental stages (L, D, DW). Each color-coded rate map is accompanied by the corresponding trajectory plots (gray lines), with color indicating event rate (yellow: maximal event rate; blue: minimal event rate).

****P ≤ 0.0001; ***P ≤ 0.001; **P ≤ 0.01; *P ≤ 0.05; ns, P > 0.05.

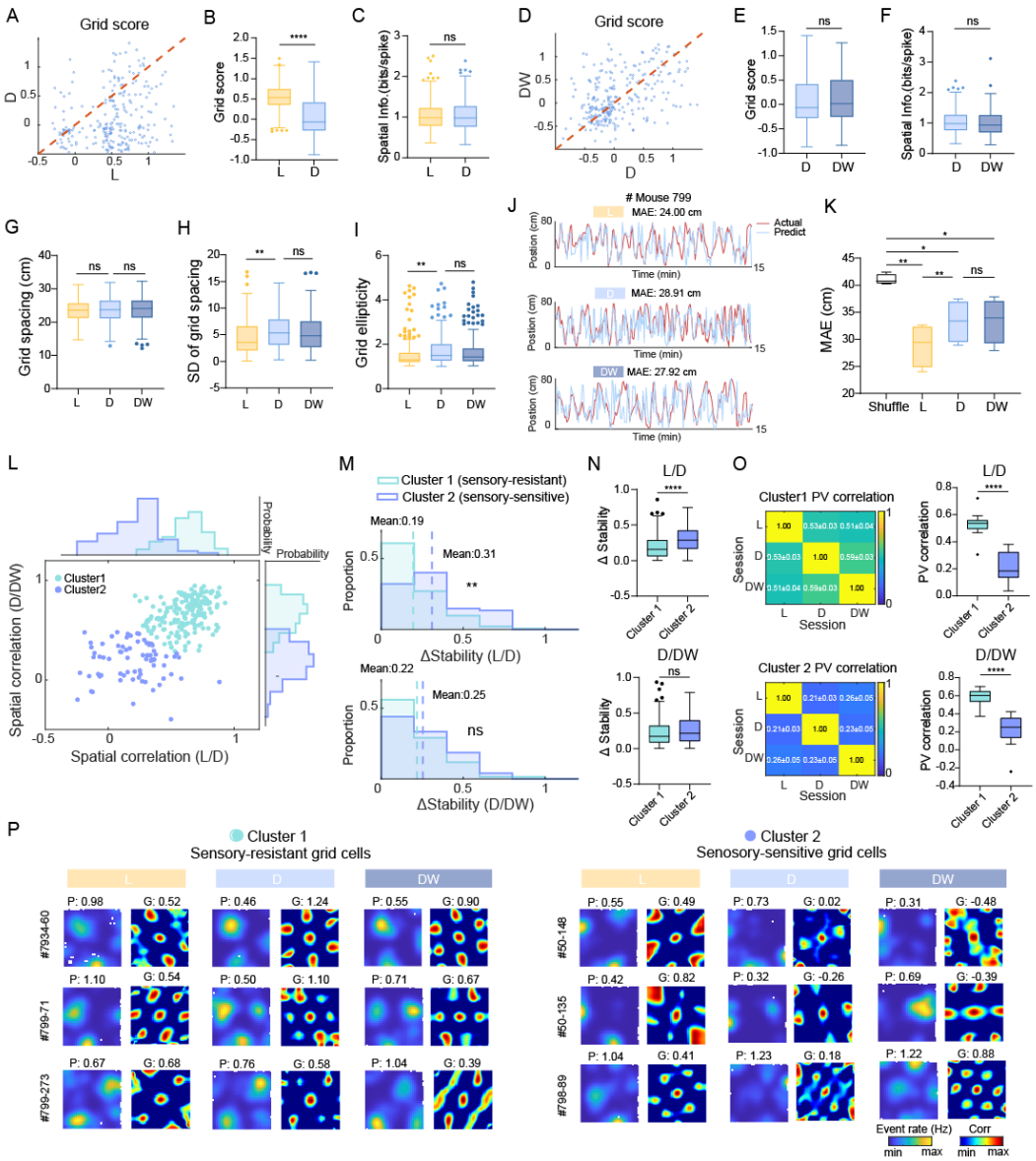

Figure 4. Spatial representation of grid cells is more influenced by light deprivation rather than by whisker trimming.

(A) Scatter plot showing distribution of grid score for all grid cells (n = 261) in Light (L) and Dark (D) conditions.

(B) Significant reduction in grid score after light deprivation (L/D) (two-sided *t*-test, P = 2.8 × 10^{-32}, n = 261).

(C) No significant change in spatial information (bits/spike) was observed from L to D (two-sided *t*-test, P = 0.70, n = 261).

(D-F) Similar analyses as in (A-C), depicting changes in grid score and spatial information after whisker trimming (D/DW) (two-sided *t*-test, grid score: P = 0.13; Spatial Info.: P = 0.09, n = 261).

(G) No significant change in average grid spacing following light deprivation (L/D) (Wilcoxon test, n = 261, P = 0.26) or whisker deprivation (D/DW) (Wilcoxon test, P = 0.64, n = 261).

(H) Significant increase in the standard deviation (SD) of grid spacing in the dark (L/D), with no further change after whisker trimming (D/DW) (Wilcoxon test, L/D: $P = 8.2 \times 10^{-5}$; D/DW: P = 0.16, n = 261).

(I) Similar to the SD of grid spacing, grid ellipticity increased in the dark, indicating a more irregular grid pattern (Wilcoxon test, L/D: P = 0.002; D/DW: P = 0.13, n = 175 for L/D, n = 180 for D/DW).

(J) Representative examples of actual versus predicted positions across the three experimental sessions, decoded from neuronal activity of all grid cells in one mouse.

(K) Mean Absolute Error (MAE) in position prediction by grid cells across different conditions, showing that the spatial representation of grid cells changes in darkness (D) compared with its original state (L). In all experimental conditions, MAE is significantly lower than in shuffled data (paired *t*-test, n = 4, Shuffle/L: P = 0.005; Shuffle/D: P = 0.02; Shuffle/DW: P = 0.02; L/D: P = 0.007; D/DW: P = 0.92).

(L) GMM clusters grid cells into two distinct clusters based on the spatial correlation of their rate maps between session pairs. Cluster 1 exhibits higher spatial correlation across L/D and D/DW sessions, while Cluster 2 shows lower spatial correlation.

(M) Distribution of within-session stability (Δ Stability) for different grid cell clusters, showing that Cluster 1 (sensory-resistant) exhibits smaller changes in stability compared to Cluster 2 (sensory-sensitive) after light deprivation (L/D) (KS-test, n = 186 and n = 75, $P = 6.3 \times 10^{-5}$), but not after whisker trimming (D/DW)(P = 0.31).

(N) Statistical analysis of Δ Stability across experimental conditions, revealing significant differences between Cluster 1 and Cluster 2 after light deprivation (L/D) (Welch's *t*-test, n = 186 and n = 75, $P = 2.4 \times 10^{-5}$), but not after whisker trimming (D/DW) (P = 0.15).

(O) Right: Correlation of population vector matrices for distinct grid cell clusters across sessions, with color-coded bins representing correlation values (yellow: high correlation, blue: low correlation). Left: Box plots show that Cluster 1 shows higher correlations across sessions compared to Cluster 2 (paired *t*-test, n = 11, L/D: $P = 7.2 \times 10^{-6}$; D/DW: $P = 5.0 \times 10^{-7}$)

(P) Representative examples of color-coded rate maps and corresponding autocorrelograms for grid cells in Cluster 1 and Cluster 2, illustrating their different responses to external sensory changes.

****P ≤ 0.0001; ***P ≤ 0.001; **P ≤ 0.01; *P ≤ 0.05; ns, P > 0.05.

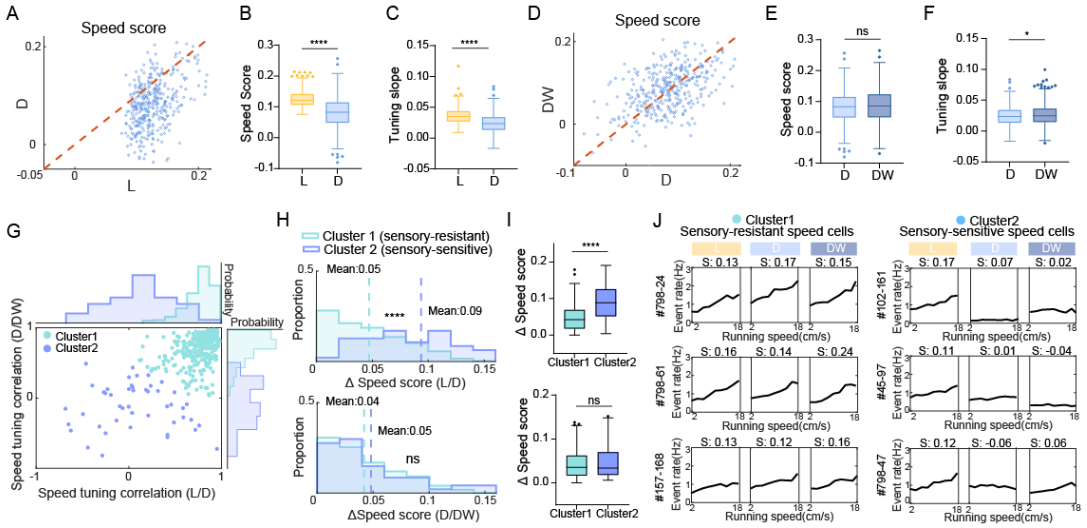

Figure 5. Speed tuning in the MEC is more affected by visual input deprivation, similar to grid cells.

(A) Scatter plot showing distribution of speed score for all speed cells (n = 363) in Light (L) and Dark (D) conditions.

(B) Significant reduction in speed score following light deprivation (L/D) (two-sided *t*-test, $P = 1.4 \times 10^{-57}$, n = 363).

(C) Decrease in the tuning slope of speed cells, indicating a reduced positive correlation between firing rate and running speed in darkness (two-sided *t*-test, $P = 2.0 \times 10^{-38}$).

(D-F) Similar analyses as in (A-C), showing no change in speed score and a slight increase in tuning slope after whisker trimming (D/DW) (two-sided *t*-test, speed score: P = 0.12; tuning slope: P = 0.01, n = 363).

(G) GMM clusters speed cells into two distinct clusters based on each cell's speed tuning correlation between session pairs. Cluster 1 (sensory-resistant) exhibits higher speed tuning correlation across sessions, while Cluster 2 (sensory-sensitive) shows lower correlation.

(H) Distribution of Δ Speed score for different clusters, showing that Cluster 1 has significantly smaller changes in Δ Speed score compared to Cluster 2 after light deprivation (L/D), but no significant difference after whisker trimming (D/DW) (KS-test, L/D: $P = 2.5 \times 10^{-7}$; D/DW: P = 0.72).

(I) Statistical analysis of Δ Speed score across experimental conditions, revealing significant differences between Cluster 1 and Cluster 2 after light deprivation (L/D) (Welch's *t*-test, L/D: $P = 4.0 \times 10^{-8}$), but not after whisker trimming (D/DW) (P = 0.32).

(J) Representative examples of speed tuning curves for sensory-resistant and sensory-sensitive speed cells across different experimental stages, showing a significant alteration in speed tuning for sensory-sensitive cells in the dark.

****P ≤ 0.0001; ***P ≤ 0.001; **P ≤ 0.01; *P ≤ 0.05; ns, P > 0.05.

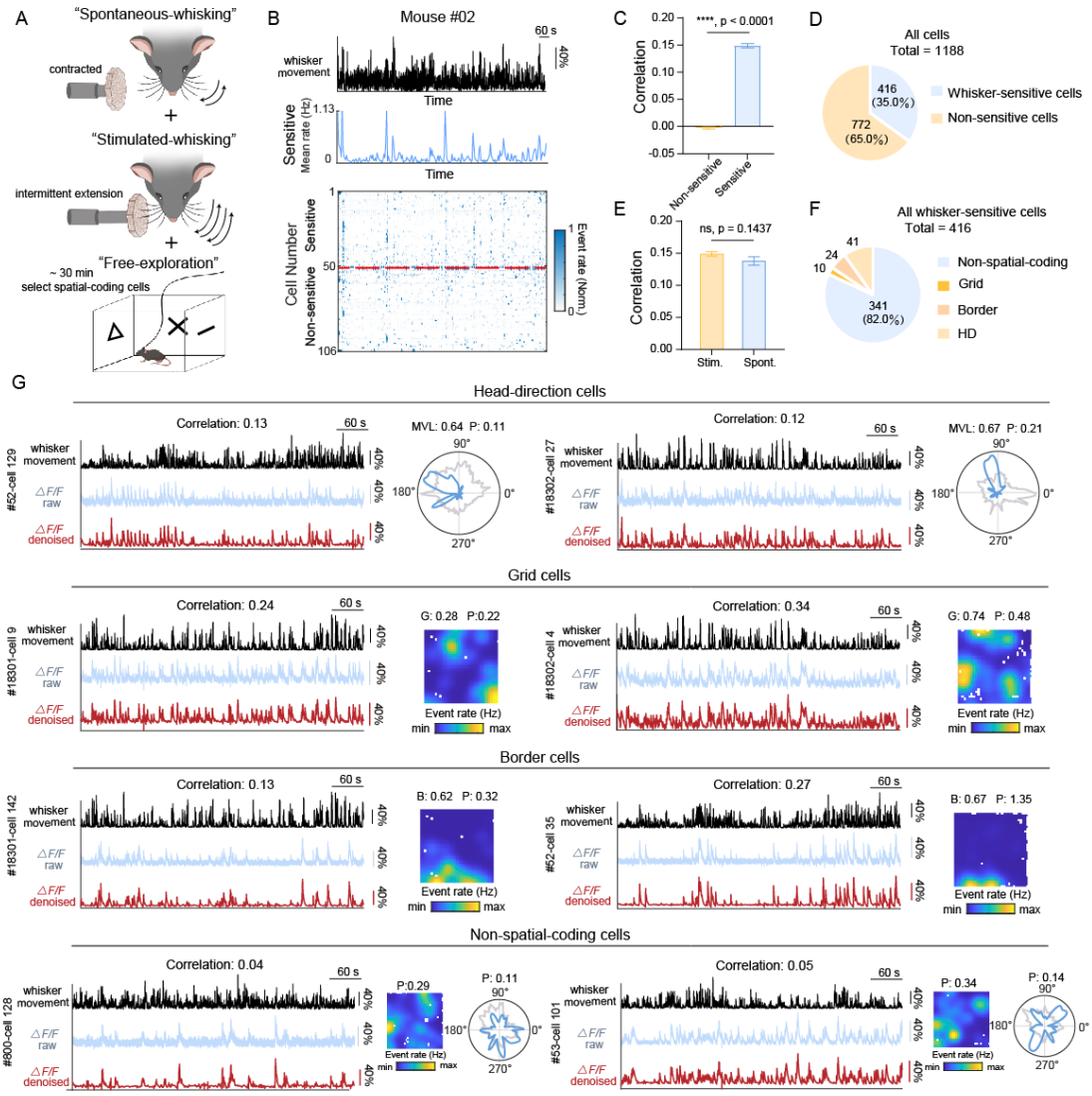

Figure 6. Identification of whisker-sensitive cells in the MEC.

(A) Experimental design and setup illustrating three whisker-related sessions: "spontaneous-whisking," "stimulated-whisking," and "free exploration." During the "stimulated-whisking" session, an automatic retractable rod was used to enhance whisker movement.

(B) Top: Whisker movements during the "stimulated-whisking" session for a representative mouse. Middle: The mean rate curve of all “whisker-sensitive” cells identified in this mouse demonstrates a high degree of consistency with whisker movement. Bottom: Heatmap showing the standardized event rate of all identified “whisker-sensitive” and “whisker-non-sensitive” cells in the same mouse, with white color indicating the lowest event rate and dark blue indicating the highest.

(C) Comparison of Pearson correlation coefficients between event rate and whisker movement for “whisker-sensitive” and “whisker-non-sensitive” cells during the "stimulated-whisking" session (Welch’s *t*-test, n = 416 and n = 772, P = 1.3×10^{-154}).

(D) Proportion of “whisker-sensitive” and “whisker-non-sensitive” cells among all recorded cells (total n = 1,188).

(E) Correlation between event rate and whisker movement of “whisker-sensitive” cells during the "spontaneous-whisking" (Spont.) session shows no significant difference compared to the “stimulated-whisking” (Stim.) session (Welch’s *t*-test, n = 416, P = 0.14).
(F) Distribution of different spatial-coding cell types among all “whisker-sensitive” cells, showing the proportions of grid, border, head direction, and non-spatial-coding cells.
(G) Examples of “whisker-sensitive” cells with or without spatial-coding properties. Top to bottom: HD cells, grid cells, border cells, and non-spatial-coding cells. The black trace represents whisker movement over time, the blue trace shows raw ΔF/F, and the red trace shows denoised ΔF/F. The right panels display the corresponding spatial firing maps or head-direction tuning curves for each cell in the “free exploration” session.
****P ≤ 0.0001; ***P ≤ 0.001; **P ≤ 0.01; *P ≤ 0.05; ns, P > 0.05.

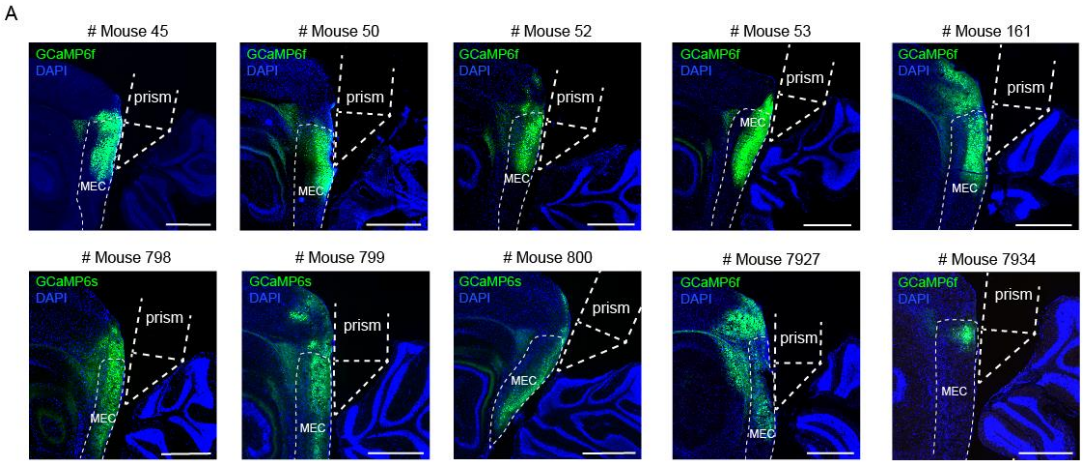

Supplementary Figure 1. Histological reconstructions of MEC-targeted imaging.
(A) Representative histological sections showing GCaMP6f or GCaMP6s expression (green) in the MEC across ten example mice. DAPI staining (blue) highlights cellular nuclei. A prism was implanted at the interface between the cortex and the cerebellum to facilitate optical access for imaging. The position of the prism is indicated by dashed lines. Scale bars represent 1 mm.

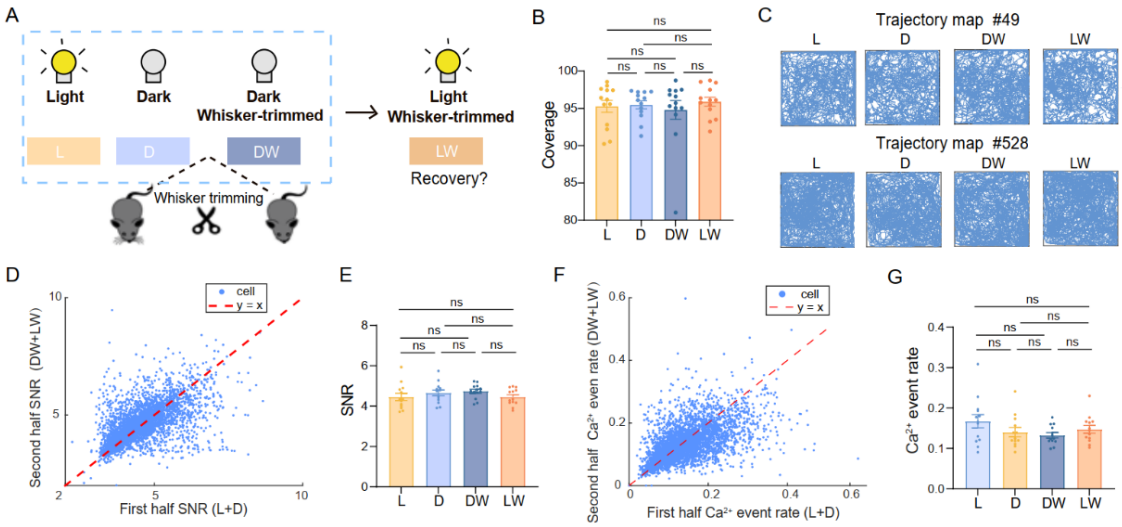

Supplementary Figure 2. Experimental design, animal behavior, and evaluation of two-photon imaging quality across sessions.

(A) Schematic of the experimental timeline. Mice were sequentially subjected to four conditions: Light (L), where mice established stable spatial representations in an open field under light conditions; Dark (D), where mice explored the same environment in darkness; Dark, Whisker-trimmed (DW), where all whiskers were trimmed before re-exposure to the same environment in darkness; and Light, Whisker-trimmed (LW), where visual cues were reintroduced by turning on the light after the animals' whiskers had been trimmed.

(B) Trajectory coverage of the open field is consistently high across all sessions (repeated measures one-way ANOVA, n = 13, P = 0.47).

(C) Representative trajectory maps of two mice, illustrating uniform exploration of the open field across all sessions.

(D) Scatter plot of signal-to-noise ratio (SNR) for all cells in the first half (L + D) versus the second half (DW + LW) of the sessions, with data points distributed around the line y = x (n = 3,758).

(E) SNR across different sessions remained stable, indicating consistent imaging quality (repeated measures one-way ANOVA, n = 13, P = 0.22).

(F) Scatter plot of average Ca^{2+} event rate for all cells in the first half versus the second half of the sessions, showing data points distributed around the line y = x (n = 3,758).

(G) Consistent Ca^{2+} event rates across sessions (repeated measures one-way ANOVA, n = 13, P = 0.09).

****P ≤ 0.0001; ***P ≤ 0.001; **P ≤ 0.01; *P ≤ 0.05; ns, P > 0.05.

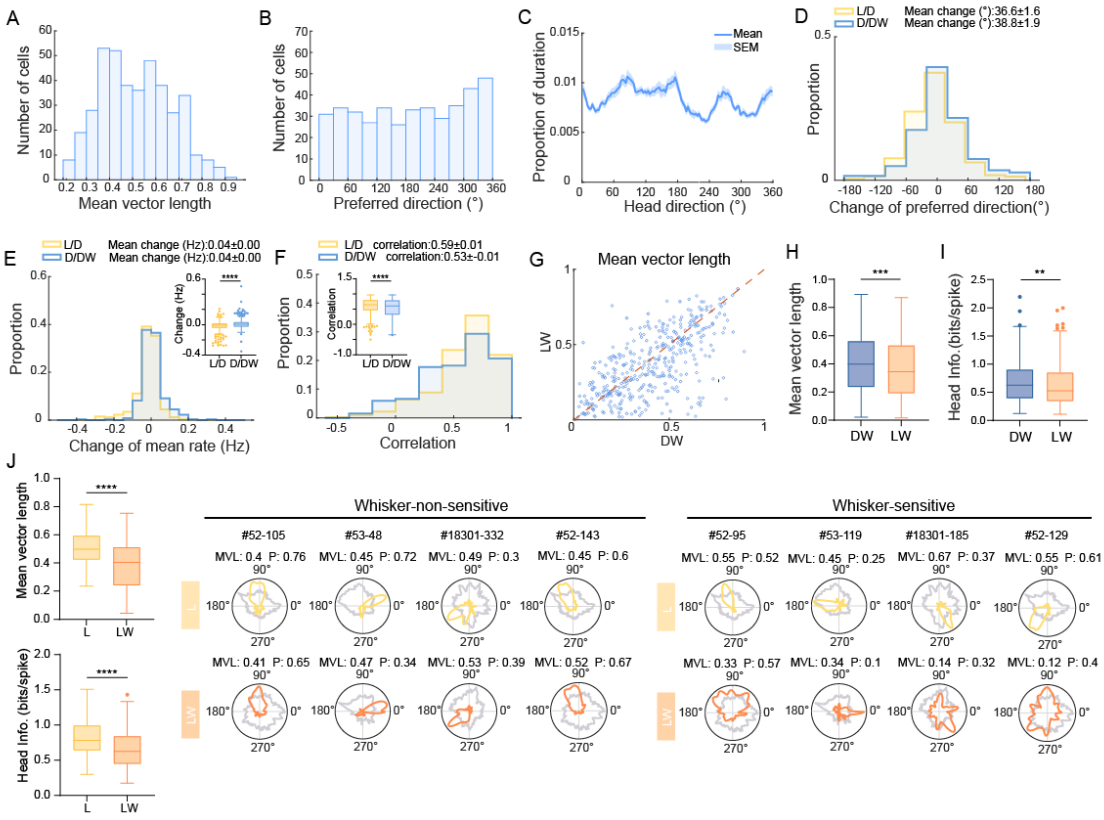

Supplementary Figure 3. Firing properties of HD cells across experimental stages and their performance in DW/LW and L-LW experiments.

(A) Distribution of mean vector length (MVL) for all HD cells during the baseline session (L).

(B) Distribution of preferred direction (PFD) for all HD cells during the light baseline session, showing nearly uniform coverage across 0-360° with slight clustering near 360°.

(C) Distribution of head direction for 13 mice during the baseline session, showing a relatively uniform distribution across 0-360°. The dark blue line represents the mean proportion at each angle, and the light blue shading indicates the standard error of the mean (SEM). The bin size for angles is 3°.

(D) Differences in the change of preferred direction (PFD) of HD cells between L/D and D/DW (KS-test, n = 406, $P = 5.8 \times 10^{-4}$). The mean change in direction for L/D and D/DW is displayed in the figure.

(E) The change in mean event rate of HD cells after whisker trimming (D/DW) is greater than light deprivation (L/D) (KS-test, n = 406, $p = 3.2 \times 10^{-4}$; Wilcoxon test, $p = 2.8 \times 10^{-7}$). The mean rate change for L/D and D/DW is shown in the figure.

(F) Distribution of correlation coefficients for HD cell tuning curves between L/D and D/DW (KS-test, n = 406, $p = 5.8 \times 10^{-4}$; Wilcoxon test, p = 0.0049). The mean correlation coefficients for L/D and D/DW are displayed in the figure.

(G) Scatter plot showing the distribution of MVL for all HD cells (n = 406) before and after the light was turned on to reintroduce visual inputs (DW/LW).

(H) Changes in the population MVL of HD cells from DW to LW. Statistical analysis was performed using a linear mixed model, two-sided *t*-test, n = 406, $p = 2.3 \times 10^{-5}$.

(I) Changes in head direction information (Head Info.) from DW to LW (two-sided *t*-test, n = 406, $p = 5.7 \times 10^{-4}$).

(J) In the L-LW experiment, HD tuning significantly decreased after whisker trimming was performed directly following the light baseline session. Left: Wilcoxon test, n = 153, MVL: $p = 3.0 \times 10^{-16}$, Head Info.: $p = 1.0 \times 10^{-10}$. Right: Examples of HD cells, showing some cells that are affected by whisker trimming (Whisker-sensitive) and others with stable MVL and PFD (Whisker-sensitive).

****$P \leq 0.0001$; ***$P \leq 0.001$; **$P \leq 0.01$; *$P \leq 0.05$; ns, $P > 0.05$.

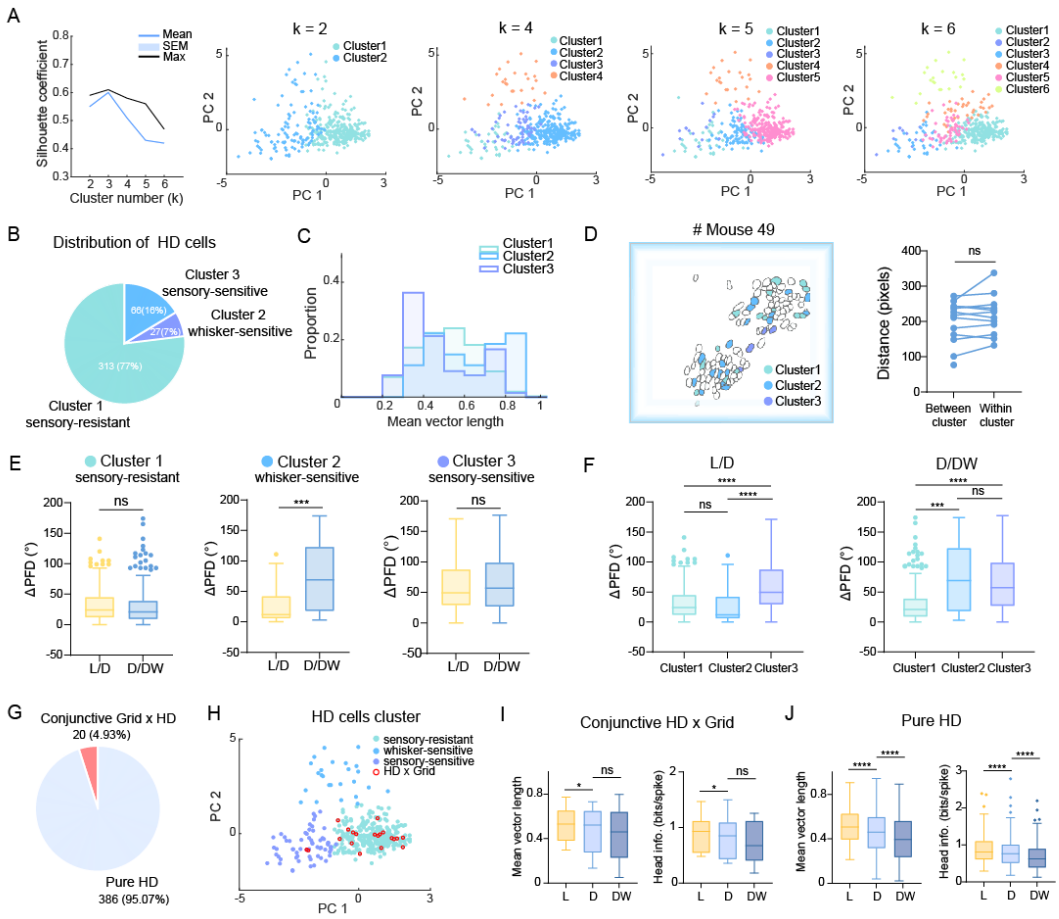

Supplementary Figure 4. Clustering of HD cells based on their sensitivity to light deprivation and whisker trimming.

(A) Silhouette analysis indicates that the optimal clustering of HD cells is achieved with three clusters. The scatter plots display the results of clustering into 2, 4, 5, and 6 groups based on the first two principal components (k = 3 results are shown in Figure 2).

(B) Proportion of each HD cell cluster.

(C) Distribution of mean vector length (MVL) during the baseline light session for each HD cell cluster (mean ± SEM). Cluster 1: 0.52 ± 0.00; Cluster 2: 0.62 ± 0.03; Cluster 3: 0.48 ± 0.02. Welch's *t*-test, P = 0.0006 (Cluster 1 vs. Cluster 2), P = 0.09 (Cluster 1 vs. Cluster 3), P = 0.0008 (Cluster 2 vs. Cluster 3).

(D) An example FOV with three HD cell clusters. Statistical analysis indicating no anatomical clustering of these HD cells. Wilcoxon test, n = 12, P = 0.47.

(E) Changes in preferred firing direction (ΔPFD) for Cluster 1 (sensory-resistant HD cells) show minimal change during both light deprivation (L/D) and whisker trimming (D/DW). Cluster 2 (whisker-sensitive HD cells) exhibit significant ΔPFD only after whisker trimming (D/DW). Cluster 3 (sensory-sensitive HD cells) display large ΔPFD across sessions. Wilcoxon test, Cluster 1: n = 313, P = 0.07; Cluster 2: P = 27, P = 3.0×10^{-4}; Cluster 3: n = 66, P = 0.92.

(F) Significant differences in ΔPFD between session pairs and HD cell clusters. After light deprivation (L/D), Cluster 3 shows significantly higher ΔPFD than Cluster 1 and Cluster 2.

After whisker trimming (D/DW), both Cluster 2 and Cluster 3 exhibit significantly higher ΔPFD than Cluster 1. Welch's *t*-test; L/D: P = 0.23 (Cluster 1 vs. Cluster 2), P = 1.0×10^{-6} (Cluster 1 vs. Cluster 3), P = 5.7×10^{-6} (Cluster 2 vs. Cluster 3); D/DW: P = 0.0003 (Cluster 1 vs. Cluster 2), P = 6.0×10^{-8} (Cluster 1 vs. Cluster 3), P = 0.38 (Cluster 2 vs. Cluster 3). These results, along with those in panel E, suggest that Cluster 1 is the most stable, Cluster 2 is affected by whisker trimming, and Cluster 3 is influenced by both sensory inputs.

(G) Proportion of conjunctive Grid × HD cells versus pure HD cells identified during the baseline session.

(H) Conjunctive Grid × HD cells are absent in the "whisker-sensitive" HD cell group.

(I) Conjunctive Grid × HD cells are more affected by light deprivation, showing characteristics similar to grid cells. Wilcoxon test, n = 20, L/D: MVL, P = 0.01; Head Info., P = 0.33; D/DW: MVL, P = 0.03; Head Info., P = 0.25.

(J) Pure HD cells are influenced by deprivation of both sensory inputs. Wilcoxon test, n = 386, L/D: MVL, P = 2.3×10^{-9}; Head Info., P = 6.2×10^{-5}; D/DW: MVL, P = 2.4×10^{-6}; Head Info., P = 6.0×10^{-9}.

****P ≤ 0.0001; ***P ≤ 0.001; **P ≤ 0.01; *P ≤ 0.05; ns, P > 0.05.

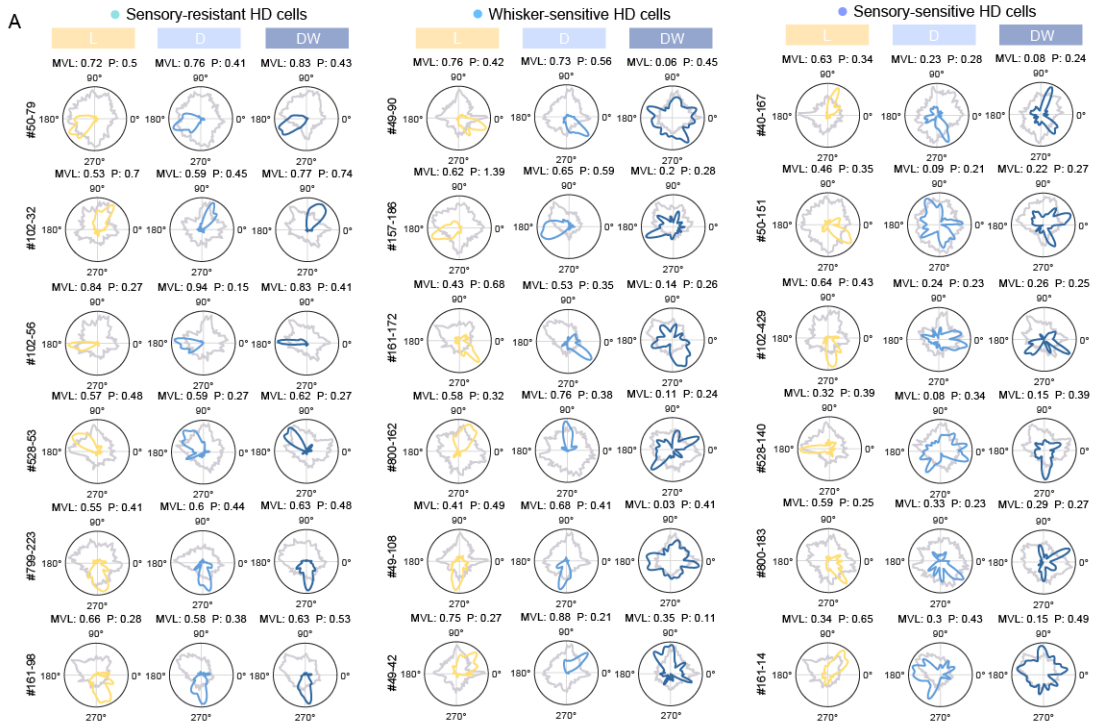

Supplementary Figure 5. Example tuning curves of distinct HD cell clusters.

(A) Tuning curves of distinct HD cell clusters across sessions showing different responses to different sensory deprivation. Left: sensory-resistant HD cells; Middle: whisker-sensitive HD cells; Right: sensory-sensitive HD cells.

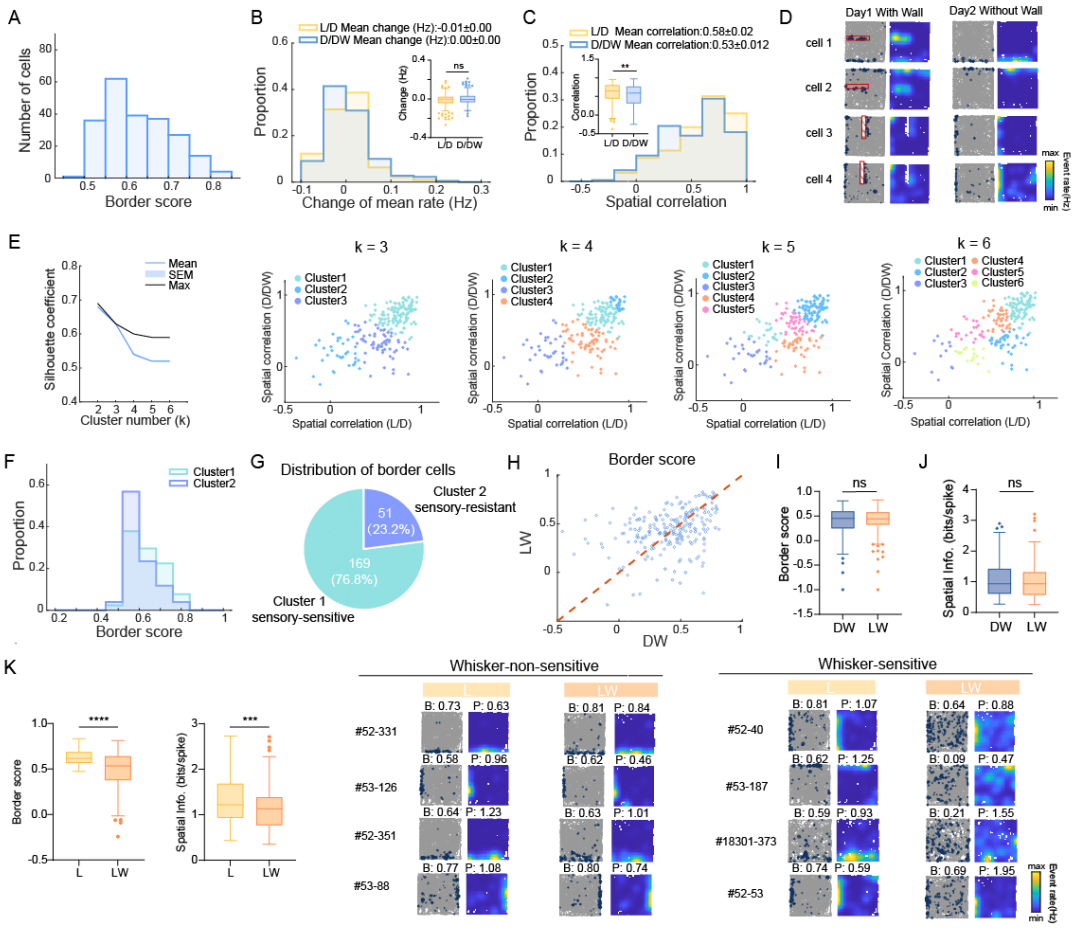

Supplementary Figure 6. Characterization of border cells and their responses in DW/LW and L-LW experiments, indicating their sensitivity to sensory input deprivation.

(A) Distribution of border score for all identified border cells during the baseline condition.

(B) Distribution histogram and statistical analysis showing no significant difference in the change of mean event rate between L/D and D/DW. KS- test, n = 220, P = 0.21; Wilcoxon test, P = 0.092. Mean change in event rate is illustrated for both conditions.

(C) Minor differences in spatial correlation of border cell rate maps between L/D and D/DW. KS-test, n = 220, P = 0.017; P = 0.0024.

(D) Verification of border cell identity by introducing a wall in the open field prior to the L-D-DW-LW experiments, demonstrating the emergence of new firing fields and confirming the presence of border cells. The red rectangle indicates the position of the inserted wall.

(E) Silhouette coefficient analysis indicates that the GMM optimally clusters border cells into two groups. Scatter plots depict clustering outcomes for k = 3, 4, 5, and 6 based on the first two principal components (k = 2 results are presented in Figure 3).

(F) Average border score of Cluster 2 is modestly higher than those of Cluster 1 during baseline condition. Mean ± SEM, Cluster 1: 0.64 ± 0.01; Cluster 2: 0.60 ± 0.01. KS-test, n = 169 (Cluster 1) and n = 51 (Cluster 2), P = 0.0053; Welch's *t*-test, P = 0.006.

(G) The proportion of each border cell cluster.

(H) Scatter plot illustrating changes in border score for all border cells (n = 220) following the reintroduction of visual inputs (DW/LW).

(I) Populational border score does not significantly recover upon re-exposure to light, as assessed by a linear mixed model analysis, two-sided *t*-test, n = 220, P = 0.48.

(J) Spatial information (Spatial Info.) remains unchanged after the restoration of visual inputs, two-sided *t*-test, n = 220, P = 0.18.

(K) In the L-LW experiment, whisker trimming following light baseline session significantly alters the spatial coding of border cells. Left: Wilcoxon test, n = 116, Border score: P = 1.1×10^{-9}; Spatial Info.: P = 3.4×10^{-4}. Right: Representative examples of some border cells displaying disrupted coding post-trimming (Whisker-sensitive) and other border cells maintaining stable coding (Whisker-non-sensitive).

****P ≤ 0.0001; ***P ≤ 0.001; **P ≤ 0.01; *P ≤ 0.05; ns, P > 0.05.

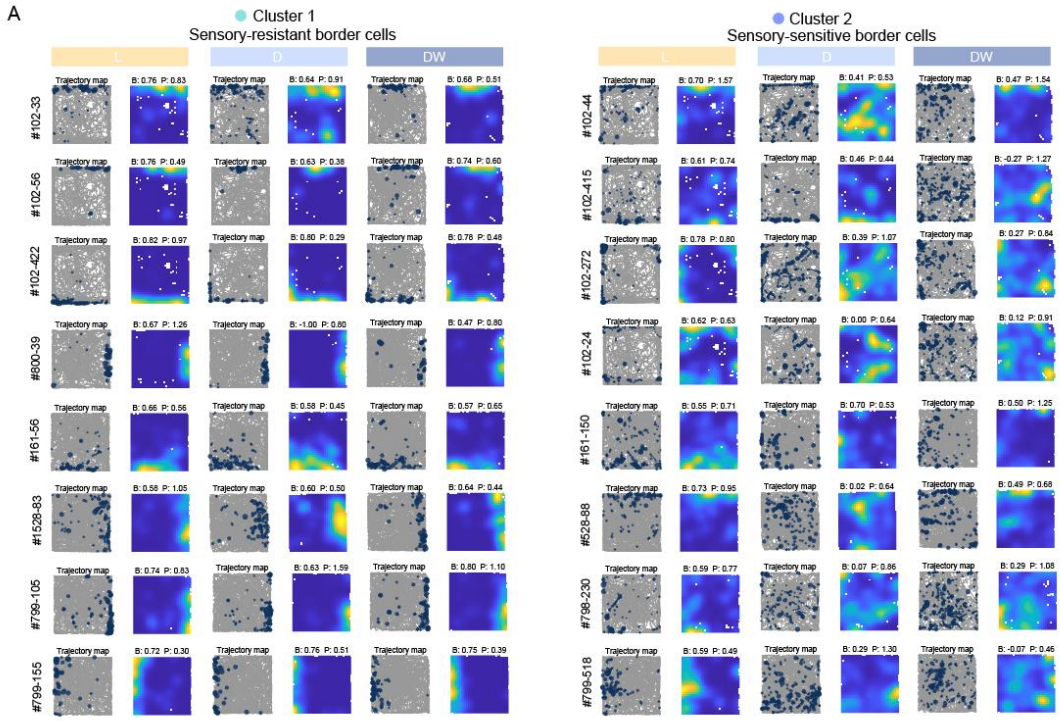

Supplementary Figure 7. Example rate maps of distinct border cell clusters.

(A) Rate maps of distinct border cell clusters across sessions showing different sensitivity to deprivation of external sensory input. Left: Sensory-resistant border cells maintain their spatial representation after sensory deprivation; Right: Sensory-sensitive border cells show deteriorated spatial representation.

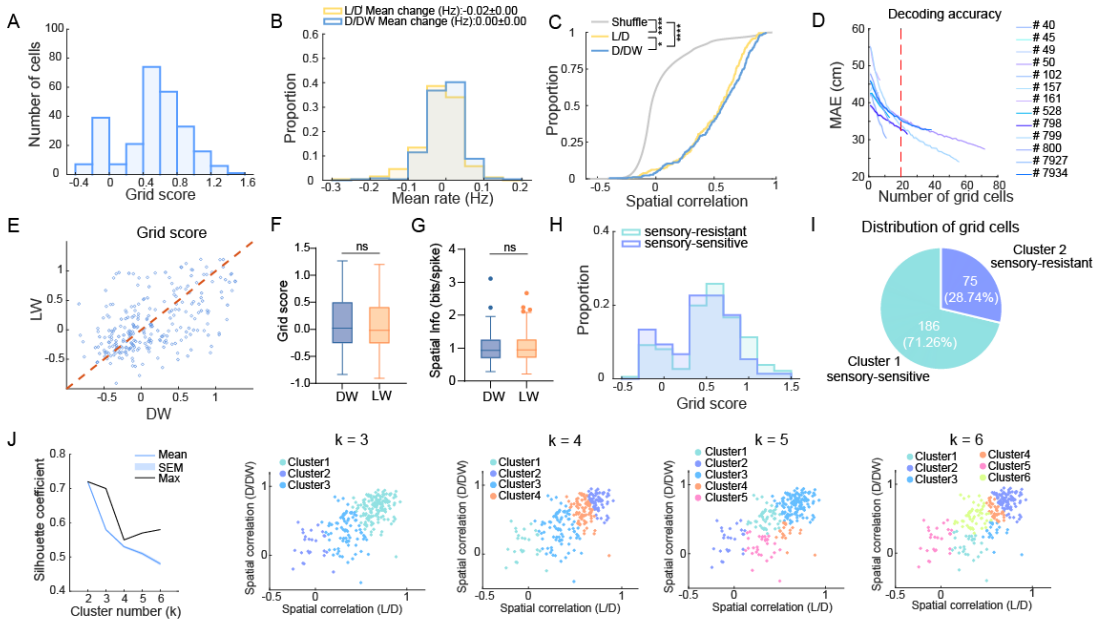

Supplementary Figure 8. Responses of grid cell under varying sensory conditions suggest a predominant influence of visual input.

(A) Distribution of grid score for all grid cells during the baseline light condition.

(B) Difference in the change of mean event rate between L/D and D/DW. KS-test, n = 261, P = 0.0028. The mean change in event rate is depicted for both conditions.

(C) Differences in spatial correlation of grid cell rate maps between L/D and D/DW, although both correlations are significantly higher compared to the shuffled condition. KS-test, n = 261, Shuffle vs. L/D: P = 2.4×10^{-111}; Shuffle vs. D/DW: P = 4.8×10^{-114}; L/D vs. D/DW: P = 0.036.

(D) Decoding accuracy improves with an increasing number of grid cells. For subsequent decoding analyses, four mice with more than 20 grid cells were selected: #50, #7934, #798, and #799.

(E) Scatter plot showing the distribution of grid score (n = 261) before and after reintroduction of visual inputs (DW/LW).

(F) Populational grid score does not significantly recover upon re-exposure to light, as assessed by a linear mixed model analysis, two-sided *t*-test, n = 261, P = 0.32.

(G) Spatial information (Spatial Info.) does not increase following the restoration of visual cues, two-sided *t*-test, n = 261, P = 0.50.

(H) No significant difference in grid score between Cluster 1 and Cluster 2 during the light baseline condition. Mean ± SEM, Cluster 1: 0.54 ± 0.03; Cluster 2: 0.44 ± 0.04. KS-test, n = 186 (Cluster 1) and n = 75 (Cluster 2), P = 0.33.

(I)The proportion of each grid cell cluster.

(J) Silhouette coefficient analysis indicates optimal clustering of grid cells into two groups. Scatter plots illustrate clustering outcomes for k = 3, 4, 5, and 6 based on the first two principal components (k = 2 results are presented in Figure 4).

****P ≤ 0.0001; ***P ≤ 0.001; **P ≤ 0.01; *P ≤ 0.05; ns, P > 0.05.

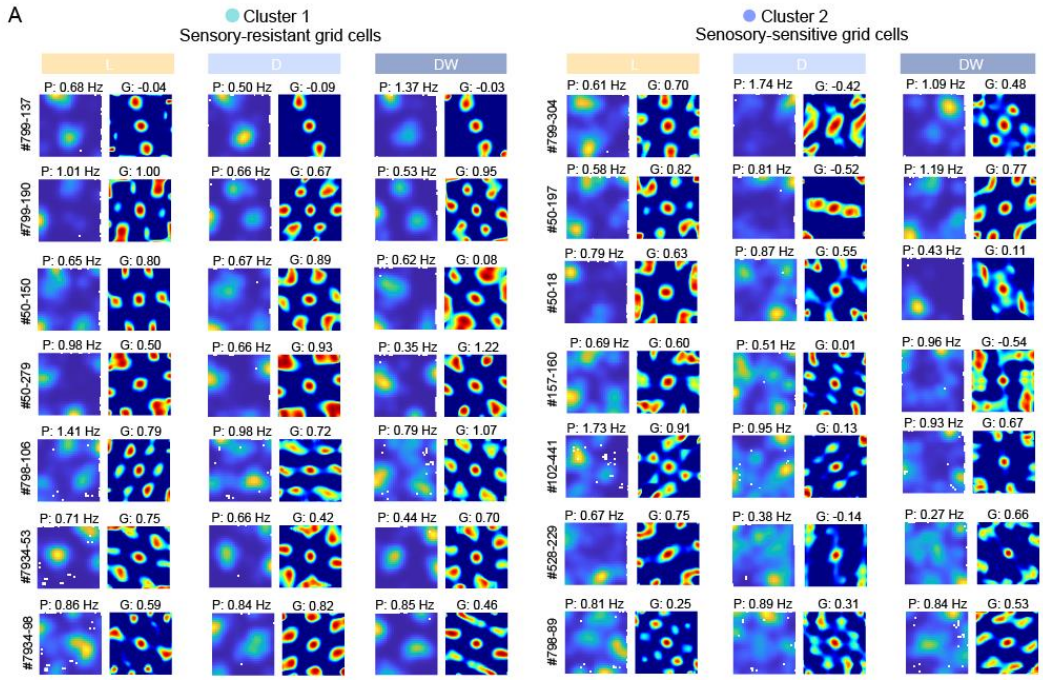

Supplementary Figure 9. Example rate maps of distinct grid cell clusters.
(A) Rate maps of distinct grid cell clusters across sessions showing their different sensitivity to deprivation of external sensory input. Left: Sensory-resistant grid cells maintain the hexagonal firing patterns after sensory deprivation; Right: Sensory-sensitive grid cells change their spatial coding after sensory deprivation.

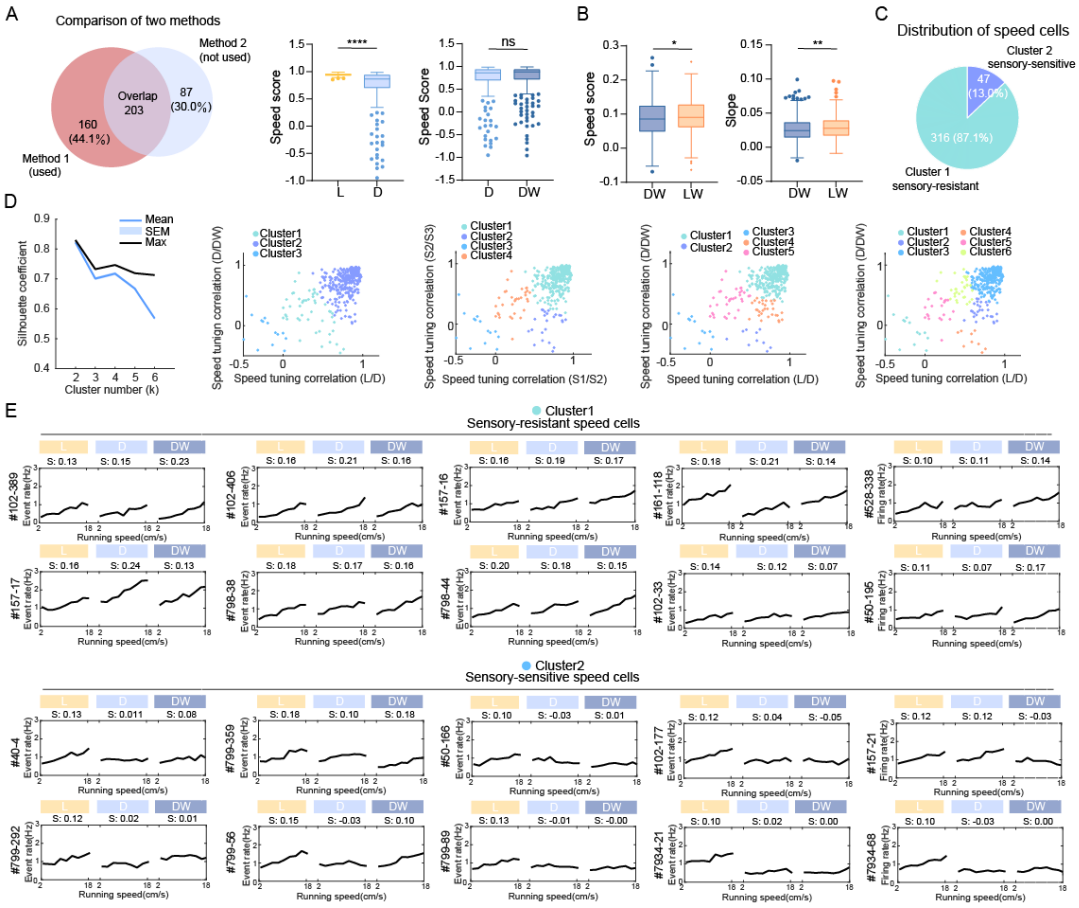

Supplementary Figure 10. Change of speed tuning in the MEC highlights the influence of visual inputs.

(A) Venn diagram comparing two methods for identifying speed cells, showing the overlap between Method 1 (used in this study) and Method 2 (not used). Method 1 identified 160 unique speed cells (44.1%), Method 2 identified 87 unique cells (30.0%), with an overlap of 203 cells (56.0%). Method 2 Speed score: n = 290, two-sided *t*-test, L/D : P = 3.8×10^{-22} D/DW: P =0.62.

(B) Box plots illustrating slight recovery of speed score after reintroducing visual inputs (DW/LW). Two-sided *t*-test, n = 363, Speed score: P = 0.013; Slope: P = 0.0010.

(C) Pie chart showing the proportion of two speed cells clusters. Cluster 1 consists of sensory-resistant cells (316 cells, 87.1%), and Cluster 2 comprises sensory-sensitive cells (47 cells, 13.0%).

(D) Silhouette coefficient analysis for clustering speed cells, with optimal clustering observed for k = 2. Scatter plots display the resulting clusters when cells are grouped into k = 3, 4, 5, and 6 clusters.

(E) Example speed tuning curves for distinct speed cell clusters.

****P ≤ 0.0001; ***P ≤ 0.001; **P ≤ 0.01; *P ≤ 0.05; ns, P > 0.05.

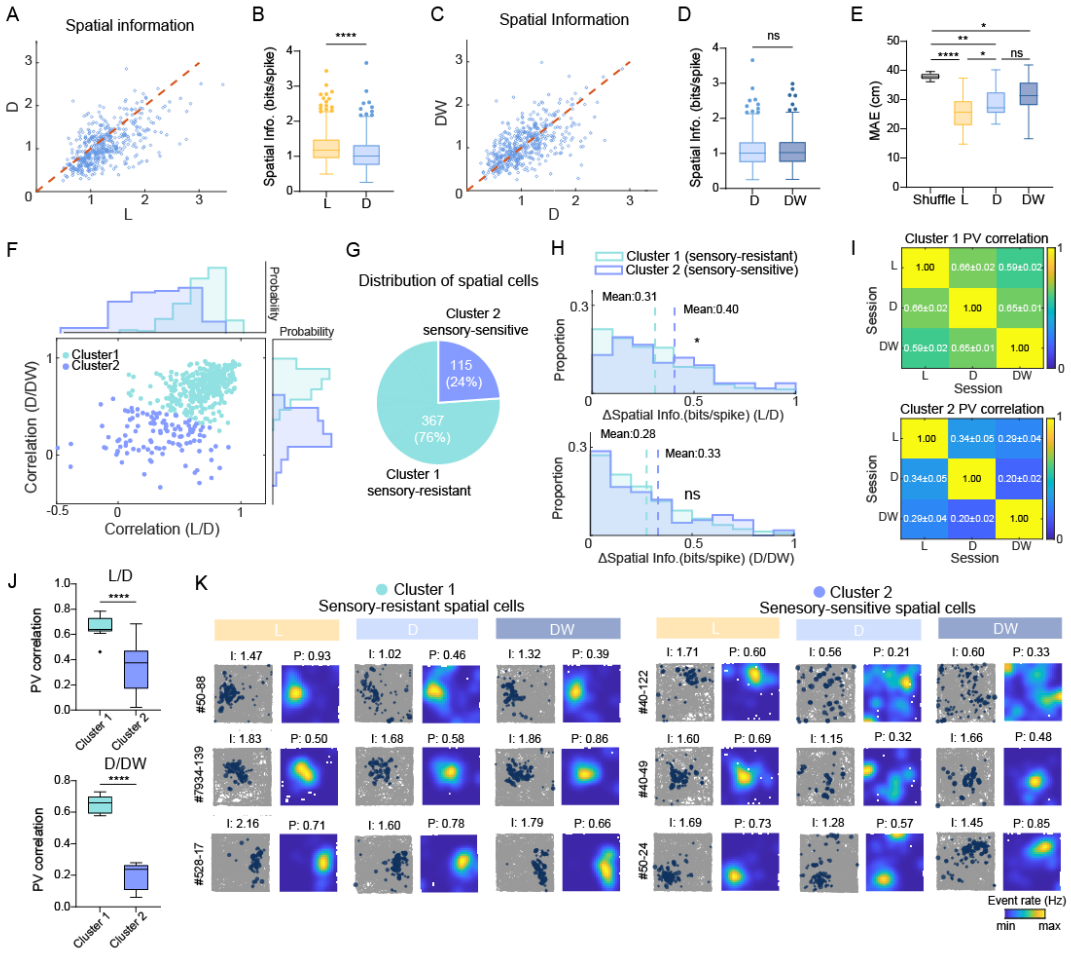

Supplementary Figure 11. Visual input predominantly governs the spatial representation of spatial cells.

(A) Scatter plot illustrating distribution of spatial information for all spatial cells (n = 482) as experimental conditions transition from Light (L) to Dark (D).

(B) Population-level changes in spatial information of spatial cells from L to D. Two-sided *t*-test, n = 482, P = 2.2×10^{-22}.

(C-D) Similar to panels A and B, these panels depict changes in spatial information following whisker trimming in the dark (D/DW). Two-sided *t*-test, n = 482, P = 0.96.

(E) Decoding accuracy of animal positions based on the neural activity of spatial cells was evaluated by training decoders on the first half of the baseline light session (L) and testing them on the second half (L), as well as on the D and DW sessions. Despite alterations in spatial representation following light deprivation (L/D), spatial decoding accuracy remained above shuffled levels across all sessions. Paired *t*-test, n = 8 mice, Shuffle/L: P = 0.0008; Shuffle/D: P = 0.0019; Shuffle/DW: P = 0.021; L/D: P = 0.023; D/DW: P = 0.093.

(F) Representative example showing actual versus predicted positions for a mouse across three experimental stages.

(G) GMM classification of spatial cells into two clusters based on spatial correlation of their rate maps across session pairs. Cluster 1 displayed higher spatial correlations between L/D and D/DW sessions, whereas Cluster 2 exhibited lower correlations.

(H) Pie chart illustrating the distribution of spatial cells into Cluster 1 (sensory-resistant, 367 cells, 76%) and Cluster 2 (sensory-sensitive, 115 cells, 24%).

(I) Cluster 1 cells show reduced sensitivity to sensory input deprivation, as evidenced by smaller changes in spatial information (Δ Spatial Info.) from L to D compared to Cluster 2. KS-test, n = 367 and n = 115, L/D: P = 0.048; D/DW: P = 0.29.

(J) Left: Correlation of population vector matrices across different sessions for Cluster 1 and Cluster 2 . The color scale reflects the strength of correlation, with yellow representing the highest and blue the lowest correlation. Right: Box plots showing a more stable population coding in Cluster1 than in Cluster 2. (paired *t*-test, n = 12, L/D: P = 6.1×10^{-6}; D/DW: P = 1.1×10^{-9})

(K) Representative examples of spatial cells from Cluster 1 (sensory-resistant) and Cluster 2 (sensory-sensitive), demonstrating their differential responses to sensory deprivation.

****P ≤ 0.0001; ***P ≤ 0.001; **P ≤ 0.01; *P ≤ 0.05; ns, P > 0.05.

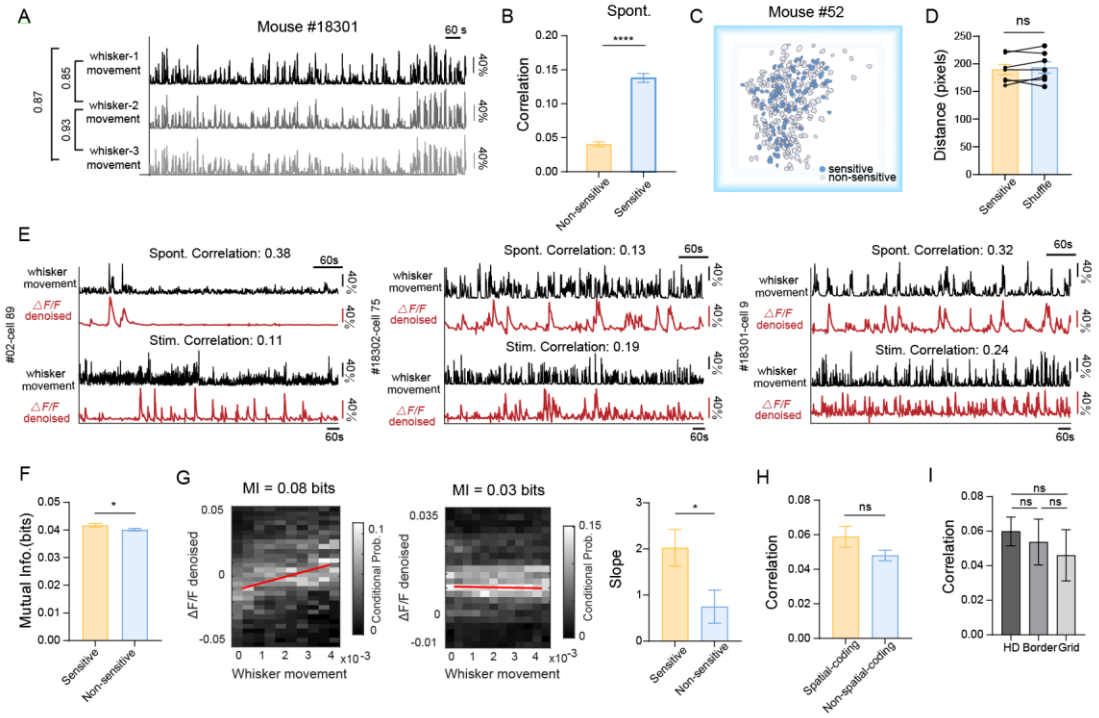

Supplementary Figure 12. MEC neurons respond to whisker movement, encompassing various spatially coding cell types.

(A) Movements of three ipsilateral whiskers in a mouse, demonstrating highly consistent whisker motion patterns.

(B) During the "spontaneous-whisking" session, neuron activity of "whisker-sensitive" cells identified in the "stimulated-whisking" phase also exhibits significantly higher correlations with whisker movement compared to "whisker-non-sensitive" cells. Welch's *t*-test, n = 772 (sensitive) and n = 416 (non-sensitive), P = 1.3×10^{-35}.

(C) Anatomical distribution of "whisker-sensitive" and "whisker-non-sensitive" cells within a field of view (FOV).

(D) "Whisker-sensitive cells" do not exhibit a clustered anatomical distribution. Wilcoxon test, n = 7 mice, P = 0.58.

(E) Representative examples of “whisker-sensitive” cells, demonstrating consistent neuronal activity correlated with whisker movement in both "stimulated-whisking" and "spontaneous-whisking" sessions.

(F) “whisker-sensitive” cells exhibit a higher mutual information (MI) than “whisker-non-sensitive” cells in “stimulated-whisking” session. Welch’s *t*-test, n = 415 and n = 772, P = 0.04

(G) Left: Examples of two cells with high and low MI. Heatmaps show conditional probability distribution of denoised ΔF/F in response to varying whisker movement intensities. Grayscale shading indicates probability, and the red line represents the linear fit between whisker movement intensity and the corresponding most likely ΔF/F values. Right: The average slope of the fitted lines is significantly steeper in "whisker-sensitive” cell populations compared to "whisker-non-sensitive” cells, indicating a stronger positive correlation between neuronal activity and whisker movement in the former. Welch’s *t*-test, n = 772 and n = 416, P = 0.018.

(H) Spatial-coding cells identified during the "free exploration" session do not show a significant difference in correlation between neuronal activity and whisker movement compared to non-spatial-coding cells. Welch’s *t*-test, n = 257 (spatial-coding) and n = 931 (non-spatial-coding), P = 0.11.

(I) No significant difference in the correlation between neuronal activity and whisker movement across different types of spatial-coding cells. Welch’s ANOVA test, n = 100 (HD cells), 76 (Border cells), and 33 (Grid cells), P = 0.71.

****P ≤ 0.0001; ***P ≤ 0.001; **P ≤ 0.01; *P ≤ 0.05; ns, P > 0.05.